




Special Section:Southern Ocean and Climate:
Biogeochemical and Physical
Fluxes and Processes**Observational Evidence of Ventilation Hotspots in the Southern Ocean**Lilian A. Dove¹ , Andrew F. Thompson¹, Dhruv Balwada² , and Alison R. Gray² ¹Division of Geological and Planetary Sciences, Environmental Science and Engineering, California Institute of Technology, Pasadena, CA, USA, ²School of Oceanography, University of Washington, Seattle, WA, USA**Key Points:**

- Observations with high spatial and temporal resolution were collected from two ocean gliders following a Biogeochemical-Argo float
- Physical and biogeochemical tracer variance is enhanced within a standing meander of the Antarctic Circumpolar Current
- The standing meander shows evidence of heightened exchange of water properties between the ocean surface boundary layer and the interior

Correspondence to:L. A. Dove,
dove@caltech.edu**Citation:**Dove, L. A., Thompson, A. F., Balwada, D., & Gray, A. R. (2021). Observational evidence of ventilation hotspots in the Southern Ocean. *Journal of Geophysical Research: Oceans*, 126, e2021JC017178. <https://doi.org/10.1029/2021JC017178>Received 10 JAN 2021
Accepted 24 JUN 2021

Abstract Standing meanders are a key component of the Antarctic Circumpolar Current (ACC) circulation system, and numerical studies have shown that these features may locally enhance subduction, upwelling, as well as lateral and vertical tracer transport. Yet, observational data from these regions remain sparse. Here, we present results based on measurements made by a group of autonomous platforms sampling an ACC standing meander formed due to the interaction of the Polar Front with the Southwest Indian Ridge. Two Seagliders were deployed alongside a Biogeochemical-Argo float that was advected through the standing meander. In the high eddy kinetic energy region of the standing meander, the glider observations reveal enhanced submesoscale frontal gradients as well as heightened tracer variability at depth, as compared to the more quiescent region further downstream. Vertical gradients in spice and apparent oxygen utilization are reduced in the standing meander despite similarities in the large-scale vertical stratification, suggesting greater ventilation of the surface ocean. These observations are consistent with numerical studies that highlight standing meanders as hotspots for ventilation and subduction due to enhanced mesoscale stirring and submesoscale vertical velocities. Our results emphasize the need to account for spatial heterogeneity in processes influencing air-sea exchange, carbon export, and biogeochemical cycling in the Southern Ocean.

Plain Language Summary The Southern Ocean plays a vital role in taking up carbon dioxide and heat from the Earth's atmosphere. Yet, historically, this region has suffered from a lack of direct observations, making it difficult to quantify rates of exchange. In regions where the strongest currents of the Southern Ocean interact with underwater topography turbulence and mixing may be locally enhanced. Data collected from two different types of robotic vehicles, including steerable ocean gliders, were used to study one of these mixing "hotspots." The instrumented platforms provided expanded data as compared to typical Southern Ocean observational techniques. The results show that these turbulent regions allow water properties, such as temperature and oxygen, to mix vigorously. In particular, at these hotspots the exchange of waters between the ocean surface and interior increases. It is important to document the magnitude and regional patterns of this exchange because only surface waters interact with the atmosphere to take up or release carbon and heat, while interior waters store these properties for centuries or longer. Numerical models of the ocean have indicated that these turbulent regions of the Southern Ocean are particularly influential, and we provide some of the first observational evidence confirming these hotspots' importance.

1. Introduction

The Southern Ocean exerts a strong control on the global climate as the primary site of both deep water ventilation at the ocean surface and subduction of newly formed intermediate water masses (Marshall & Speer, 2012). Tilted density surfaces spanning the Antarctic Circumpolar Current (ACC) expose a range of density classes at the ocean surface, causing the Southern Ocean to be a key site for the uptake and sequestration of anthropogenic carbon dioxide from the atmosphere (Frölicher et al., 2015; Gruber et al., 2019). Observations in the Southern Ocean have historically been both spatially and temporally sparse, contributing to disagreements between carbon uptake estimates in models and observations (Gruber et al., 2019) and limiting attribution to specific processes that explain these discrepancies. The deployment of Biogeochemical-Argo (BGC-Argo) floats as part of the Southern Ocean Carbon and Climate Observations and Modeling (SOCCOM) project, which began in 2014, has started to fill the gap in observations of biogeochemical tracers, especially in winter months (Gray et al., 2018; Johnson et al., 2017; Riser et al., 2016). The typical

float sampling strategy of repeat profiling every 10 days maximizes the temporal and spatial coverage of the resulting data set, at the cost of aliasing mesoscale and submesoscale dynamics that can have a leading order impact on larger-scale Southern Ocean properties (Rintoul, 2018). Due to the lack of high-frequency subsurface observations, the impact of mesoscale and submesoscale processes on modulating biogeochemical tracer distributions in the Southern Ocean remains largely unresolved.

Export production, the flux of net primary production across the base of the ocean's euphotic zone, is a critical step for the sequestration of carbon from the atmosphere into the deep ocean (Buesseler & Boyd, 2009; Levy et al., 2013; Sallée et al., 2012). Our appreciation of the complexity of the organic carbon pump has expanded in recent years (Boyd et al., 2019), making it clear that the vertical carbon flux associated with gravitational sinking alone is insufficient to close the carbon budget (Boyd et al., 2019; Levy et al., 2013; Schlitzer, 2002). Ecological processes (e.g., predator migration) and physical processes have both been highlighted as potential mechanisms for enhancing carbon export fluxes (Lévy et al., 2012, 2018; Omand et al., 2015). Physical processes that contribute to nongravitational carbon export are associated both with modulation of mixed layer depths (MLDs) and with direct transport by vertical motions across the base of the mixed layer. The MLD changes in response to wind and buoyancy forcing, the latter caused by surface heating, freshwater fluxes, or sea ice melt that act dominantly at seasonal timescales with contributions from processes occurring at higher-frequency timescales as well (Bol et al., 2018; Dall'Olmo et al., 2016; Pavlevsky et al., 2016). Export may also occur via subduction processes at frontal zones due to associated strong vertical velocities (Klein & Lapeyre, 2009). The three-dimensional (3D) overturning structure and energetic eddy field of the Southern Ocean preconditions this region to have a significant contribution to export from physical processes (Llort et al., 2018; Omand et al., 2015).

Assessment of the potential for physical export in the Southern Ocean must account for the multi-scale nature of the circulation. At larger scales, the ACC is comprised of a series of eastward-flowing frontal jets that are typically efficient water mass barriers (Orsi et al., 1995). These frontal flows are accompanied by strongly tilting density surfaces in thermal wind balance that allow for the adiabatic ventilation of deep waters and sustain a vigorous mesoscale eddy field (Rintoul & Naveira Garabato, 2013). A small number of standing meanders form in the ACC where these jets interact with major topographic features, including one arising from the flow of the Polar Front (PF) over the Southwest Indian Ridge (SWIR). This standing meander is the focus of this study (Figure 1). In these standing meander regions, flow-topography interactions can cause transport barriers to become “leaky” (Naveira Garabato et al., 2011) as well as enhance eddy kinetic energy (EKE) (Gille & Kelly, 1996; Witter & Chelton, 1998; Lu & Speer, 2010), vertical momentum transport (Thompson & Naveira Garabato, 2014), lateral tracer transport (Dufour et al., 2015; MacCready & Rhines, 2001; Roach et al., 2016; Thompson & Sallée, 2012), upwelling (Tamsitt et al., 2017; Viglione & Thompson, 2016), and subduction (Bachman & Klocker, 2020; Llort et al., 2018). Observational studies of the circulation in the SWIR region, for example, Pollard and Read (2001), have identified a steady, largely barotropic jet associated with the PF, which is stabilized by the ridge before “fragmenting” into multiple smaller-scale jets further downstream. This area plays a central role in the upwelling branch of the overturning circulation (Tamsitt et al., 2017).

ACC standing meanders are characterized by enhanced EKE and strain rates due to persistent conditions favorable for baroclinic and barotropic instabilities (Lu et al., 2016; Youngs et al., 2017). The imprint of coherent eddies on tracer structure, for example, surface chlorophyll, occurs over horizontal scales of $O(10\text{--}100\text{ km})$. These eddies typically have a vertical extent of $O(2,000\text{ m})$ and stir tracers below the mixed layer in the interior (Balwada et al., 2016, 2020). Near the surface, mesoscale eddies usually have an inlay of strong submesoscale $O(1\text{--}10\text{ km}, 1\text{ h}\text{--}10\text{ days})$ currents, which are often visible as cusps and filaments in surface tracers. These smaller scale motions are energized by the production of surface buoyancy gradients through mesoscale frontogenesis (Adams et al., 2017; Klein & Lapeyre, 2009) and by the formation of submesoscale eddies through mixed layer baroclinic instabilities (Boccaletti et al., 2007) or through wind-front interactions (Thomas et al., 2008). Submesoscale currents are generally associated with elevated vertical velocities and restratification tendencies in the mixed layer (Su et al., 2018). Strong vertical velocities may penetrate up to a few 100 m below the base of mixed layer (Siegelman et al., 2020), playing an important role in transporting material across the base of the mixed layer and connecting the surface ocean to the mesoscale-dominated interior.

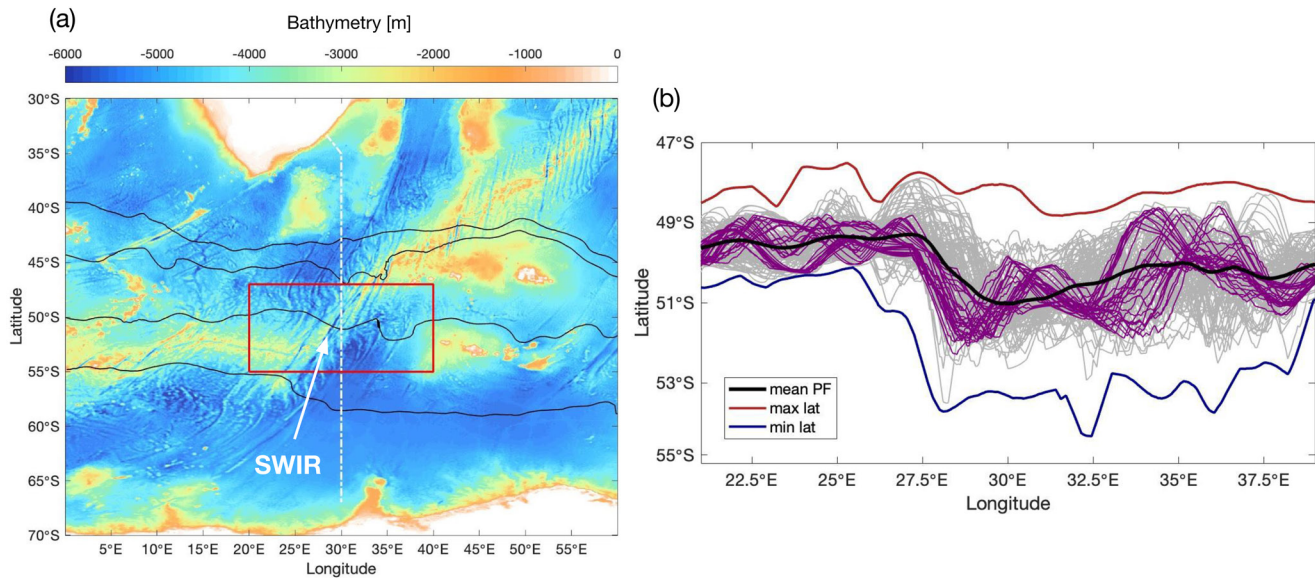


Figure 1. Standing meander location. (a) Bathymetry of the western Indian sector of the Southern Ocean. The white dotted line shows the path of the I6S GO-SHIP cruise track; the red box outlines the study region shown in panel (b). Thin black lines denote the major fronts of the Antarctic Circumpolar Current as defined in Gray et al. (2018). Southwest Indian Ridge is labeled as SWIR. (b) Latitude of the sea surface height contour corresponding to the Polar Front (PF) as defined by Kim and Orsi (2014). Gray lines show weekly examples from 2017 to 2020, and the black line shows the mean location. Purple lines show examples of the PF location from every 3 days during the glider deployment timeframe (April 29–July 25, 2019). Blue and red lines are the maximum and minimum latitudinal extents of the PF, respectively.

Both observational and modeling studies have confirmed that the Southern Ocean has an active submesoscale flow field (Adams et al., 2017; Bachman et al., 2017; du Plessis et al., 2017, 2019; Rosso et al., 2014; Viglione et al., 2018), although the degree to which submesoscale motions are effective at enabling surface-interior exchange has been limited to modeling studies (Balwada et al., 2018; Brannigan, 2016; Mahadevan, 2016; Uchida et al., 2019). In some regions, strong upper-ocean vertical stratification, often induced by sea-ice melt in the marginal ice zone, may limit the vertical extent of submesoscale motions (Swart et al., 2020). However, observations in a region of vigorous EKE and mesoscale strain further to the north have been used to infer enhanced vertical velocities well below the ocean surface (Siegelman et al., 2019). Constraining the impact of submesoscale dynamics on vertical tracer exchange from observations requires high spatial- and temporal-resolution measurements that are challenging to acquire, particularly in regions with a strong mean flow. Inhomogeneity in submesoscale variability is a key feature of the Southern Ocean that appears to be strongly shaped by interactions with topography (Rosso et al., 2015; Viglione et al., 2018).

Tracer variability arising from mesoscale is difficult to distinguish from that caused by submesoscale dynamics, and previous modeling work has demonstrated the close link between these scales. Increasing model resolution leads to the production of more small-scale features, but they remain structured around the mesoscale eddy field (Balwada et al., 2018). Mesoscale strain has also been shown to be a proxy for the magnitude of submesoscale vertical velocities (Rosso et al., 2015; Siegelman et al., 2020). The entangled nature of mesoscale and submesoscale flows, together with the 3D nature of the currents, means that while fine-scale structure in tracer variability is a well-known feature of the Southern Ocean (Joyce et al., 1978; Pollard & Read, 2001), attribution of this structure to specific dynamical processes remains challenging.

The primary goal of the Southern Ocean Glider Observations of Submesoscales (SOGOS) project was to observe the variability of physical and biogeochemical properties around a BGC-Argo float at much higher spatial and temporal resolution than the typical float sampling, through the use of two ocean gliders. Details of the autonomous platforms and their sampling capabilities are provided in Section 2, and the measurements collected by these platforms that are used to examine the influence of mesoscale and submesoscale processes on ventilation are presented in Section 3. Section 4 considers these measurements in the context of recent numerical simulations and shows that the observational evidence supports the hypothesis that ACC standing meanders are sites of enhanced Southern Ocean ventilation. We conclude in Section 5 by

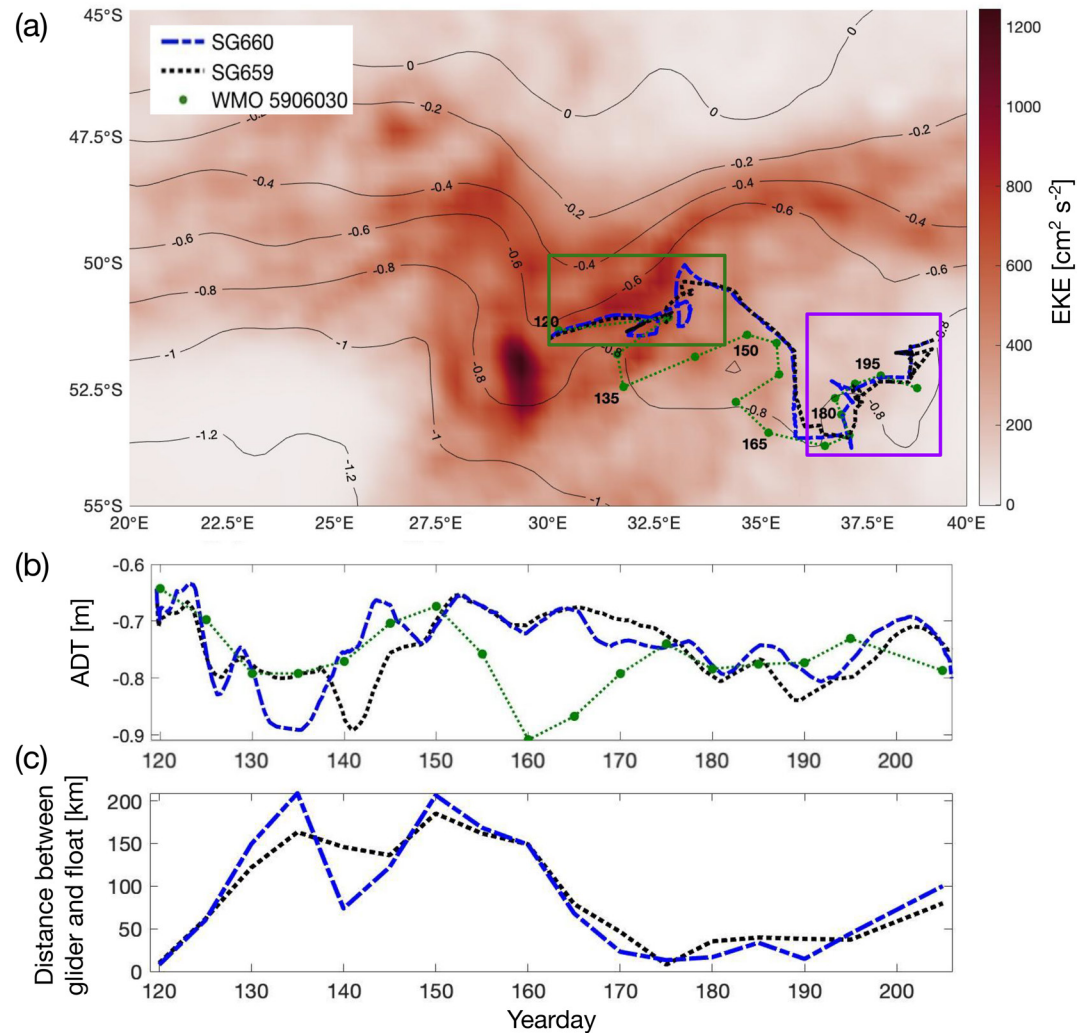


Figure 2. Study region. (a) Mean eddy kinetic energy (EKE; [$\text{cm}^2 \text{s}^{-2}$]) from 2017 to 2020 in the same area as boxed in Figure 1a. Gray contours give the mean absolute dynamic topography (ADT) from AVISO over the same time period, ranging from -1.2 to 0 m with 0.2 m increments. Lines represent the paths of ocean gliders SG660 (blue) and SG659 (black) and the profile positions of float WMO 5906030 are denoted by green points. Numbers represent the yearday when the float performed a vertical profile. Green box represents the high-eddy kinetic energy (EKE) region and purple box represents the low-EKE region as discussed in the text. (b) Absolute dynamic topography values at the locations of the float and glider profiles. Although the gliders were persistently north of the float during the early stages of the deployment, they sampled similar water masses as indicated by their proximity in sea surface height space. (c) Distance (km) between each of the two gliders and the float.

suggesting how these results inform sampling strategies of future Southern Ocean observing systems (Meredith et al., 2013) as well as our ability to monitor future changes to the Southern Ocean carbon sink.

2. Data and Methods

2.1. Autonomous Platforms and Sensors

The SOGOS field campaign began with the deployment of two Seagliders (SG659 and SG660) in conjunction with a SOCCOM BGC-Argo float (WMO 5906030) on May 1, 2019 at 51.49°S , 30.03°E , from the I06S GO-SHIP cruise (April-May 2019, www.go-ship.org). All platforms were advected downstream to the east, experiencing meridional deviations due to flow meanders. The float and gliders sampled immediately in the lee of the SWIR, a major topographic feature in the western Indian sector of the Southern Ocean; the observation region fell roughly between 30° – 40°E and 50° – 54°S (Figure 2). The gliders sampled for a period of

86 days, ending their mission on July 25, 2019. SG659 and SG660 completed 462 and 509 V-shaped profiles from the surface to 1,000 m and back, respectively, with 3–5 h (average 4.5 h) and 2–4 km (average 3.25 km) between surfacings. The BGC-Argo float has continued to profile since deployment and remains active as of the submission date of this manuscript. During the dedicated SOGOS period, the float sampled at 5-days intervals, completing 16 vertical profiles. The drifting depth of the float was 1,000 m, and the profile depth alternated between 2,000 and 1,000 m during the 5-days interval sampling.

The SOCCOM BGC-Argo profiling float was equipped with a suite of sensors to collect profiles of physical and biogeochemical properties in the upper 2,000 dbar. A standard conductivity-temperature-depth (CTD) sensor (SeaBird 41CP) recorded bin-averaged salinity, temperature, and pressure at 2-m vertical resolution above 1,000 m and 100-m vertical resolution below. Dissolved oxygen concentrations were measured with an Aanderaa 4330 optode (Tengberg et al., 2006) at variable vertical resolution, and these data were calibrated using float-based observations of atmospheric oxygen (Johnson et al., 2015). The float detected chlorophyll fluorescence and optical backscatter at 700 nm with a WET Labs FLBB (Haëntjens et al., 2017). Nitrate and pH were also measured using an ultraviolet spectrophotometer (Johnson et al., 2013) and an ion-sensitive field effect transistor (Johnson et al., 2016), respectively, although those data are not used in the present study.

The gliders each carried unpumped CTD (CT-Sail) sensors measuring conductivity (salinity), temperature, and pressure; an Aanderaa oxygen optode; and a WET Labs ECO puck that measured induced fluorescence and optical backscatter. The salinity and temperature data from the glider sensors were calibrated to deep (>600 m) values from a ship-based profile taken during the congruous I06S GO-SHIP cruise at the deployment site. Calibration of the gliders to the float was performed when the gliders and float were within 10 km of each other. No sensor drifts were observed but pressure-dependent offsets of the temperature and salinity were used for each glider. Oxygen measurements were collected over the full 1 km dive depth; to conserve battery power, optical measurements were collected down to 400 m with occasional dives down to 1 km to determine a background signal. Oxygen measurements were calibrated with reference to the float when the float and each glider were within 10 km of each other. Only deep (>600 m) waters were used for calibration to account for surface variability and used to calculate a gain correction for the glider oxygen, similar to the method pioneered in Johnson et al. (2015). A pressure correction was also applied to the gliders' oxygen measurements below the mixed layer.

Optical backscatter data on the gliders were measured at two wavelengths: 470 and 700 nm. Raw sensor counts were calibrated using the manufacturer-supplied scale factor and dark counts. The resulting volume scattering function includes scattering signal from pure seawater and particulate scattering (Zhang et al., 2009; Vaillancourt et al., 2004). The scattering by seawater was calculated using a function described in Zhang et al. (2009) and subtracted from the volume scattering function. The resulting particulate volume scattering function was converted into particulate optical backscattering coefficient b_{pp} (Bol et al., 2018; Briggs et al., 2011). Finally, following Briggs et al. (2011), the backscatter data were filtered using a seven-point minimum filter followed by a seven-point maximum filter in order to remove spikes, which often occur in profiles of b_{pp} due to aggregate material.

Glider data were objectively mapped onto a regular grid with 10-m depth resolution along the vertical axis and 500-m distance resolution along the horizontal axis, using a Gaussian weighting function with a vertical scale of 20 m and a horizontal scale of 5,000 m. A visual comparison of the raw data to the objectively mapped data set revealed no significant biases due to this choice of resolution. The time associated with each glider position was interpolated to the horizontal distance grid to give an along-track time in number of days since January 1, 2019.

Several additional quantities were derived from the measured properties. Potential density and spice, a variable most sensitive to isopycnal thermohaline variations and least correlated with the density field, were calculated from temperature and salinity using the Thermodynamic Equation of Seawater 2010 (McDougall & Barker, 2011). Adjacency of positive (warm, salty) and negative (cold, fresh) spice anomalies can be used to identify thermohaline intrusions. The MLD was defined by a density difference criteria of 0.05 kg m^{-3} from a 10-m reference level. We follow the methods of previous work (Thompson et al., 2016; Viglione et al., 2018) to calculate the Ertel Potential Vorticity (PV) from the glider data, estimated here as

$$PV \approx fN^2 - M^4 f^{-1}, \quad (1)$$

where $N^2 = b_z$, $M^4 = b_x^2$, and $b = g\rho_0^{-1}(\rho_0 - \rho)$. Here, ρ is potential density and subscripts indicate partial derivatives and x is in the along-glider-trajectory direction. Discussion of the assumptions and limitations associated with estimating PV from glider data using Equation 1 is described in detail in the aforementioned studies. From the biogeochemical measurements, apparent oxygen utilization (AOU) was calculated as the difference between the measured oxygen and the oxygen saturation value for a given salinity and potential temperature.

2.2. Additional Data Sets

Hourly estimates of surface forcing fields for the region during the study period were obtained from the ERA-5 atmospheric reanalysis (data DOI: <http://doi.org/10.24381/cds.bd0915c6>). Net surface heat flux was calculated as the sum of the shortwave, longwave, sensible, and latent heat flux estimates. Surface freshwater flux was computed using the total precipitation and evaporation estimates. Surface wind stress was calculated using the 10 m winds (u_{10}, v_{10}) and a simple drag law; $\tau = \rho C_d U^2$, where $\rho = 1.225 \text{ kg m}^{-3}$ is the air-density, $C_d = 0.00125$ is the drag coefficient (set constant here for simplicity), and U^2 is the square of the wind speed. The zonal and meridional components of the wind stress were calculated as $\tau_x = \tau(u_{10}U^{-1})$ and $\tau_y = \tau(v_{10}U^{-1})$.

Daily estimates of sea surface height (SSH) relative to the geoid for the time period 2017–2020 were obtained from the L4-gridded satellite altimeter product provided by Aviso+ (<https://www.aviso.altimetry.fr/en/data.html>), along with u' and v' , the zonal and meridional geostrophic velocities associated with the time-varying, anomalous component of the SSH field. Regional EKE was calculated as $EKE = \frac{1}{2}\sqrt{u'^2 + v'^2}$. The mean was computed over the period 2017–2020, although the magnitude and spatial pattern of EKE did not vary significantly from year to year. SSH, represented by absolute dynamic topography (ADT), is determined as the sum of the time-mean dynamic topography and time-varying sea level anomaly. ADT values at the glider and float locations were determined using the satellite gridpoint closest to the surfacing location of the instrument.

3. Results

3.1. Regional Variability

We first describe the large-scale variability within the study region, with an emphasis on how the sampling of the autonomous platforms during the SOGOS mission fits into that broader picture. As noted above, the circulation in this area is dominated by the standing meander that forms through the interaction of the PF with the SWIR (Figure 1). The meridional variability of the PF immediately downstream of the SWIR (based on satellite observations following the methods of Kim & Orsi, 2014) illustrates that the frontal position is relatively constant upstream of the SWIR as compared to just downstream (Figure 1b). The downstream variability is consistent with a breakdown of the zonal flow and the formation of mesoscale eddies. Mean EKE accordingly reaches a local maximum within the standing meander (Figure 2a).

All SOGOS platforms spent most of their time sampling close to the PF in waters collocated with SSH values of ~ -0.7 m, hereafter referred to as PF core waters (Figure 2b). Within these waters, the gliders and float captured two distinct flow regimes. The mean EKE within the standing meander portion (between 30° – 33° E and 50° – 52° S) was $460 \text{ cm}^2 \text{ s}^{-2}$, over an order of magnitude larger than the $20 \text{ cm}^2 \text{ s}^{-2}$ average value in the region downstream where eddy activity was weak (between 35° – 40° E and 52.5° – 54° S; Figure 2a). Vigorous currents dominated the first part of the deployment in the high-EKE region near the standing meander (yeardays 120–155), which presented challenges for keeping the autonomous platforms together (Figure 2c). In the low-EKE region downstream, during the latter portion of the deployment (yeardays 170–206), the gliders sampled across at least one coherent eddy and the gliders and float remained in close proximity (Figure 2c). Throughout the sampling period, the air-sea heat flux was characterized by net

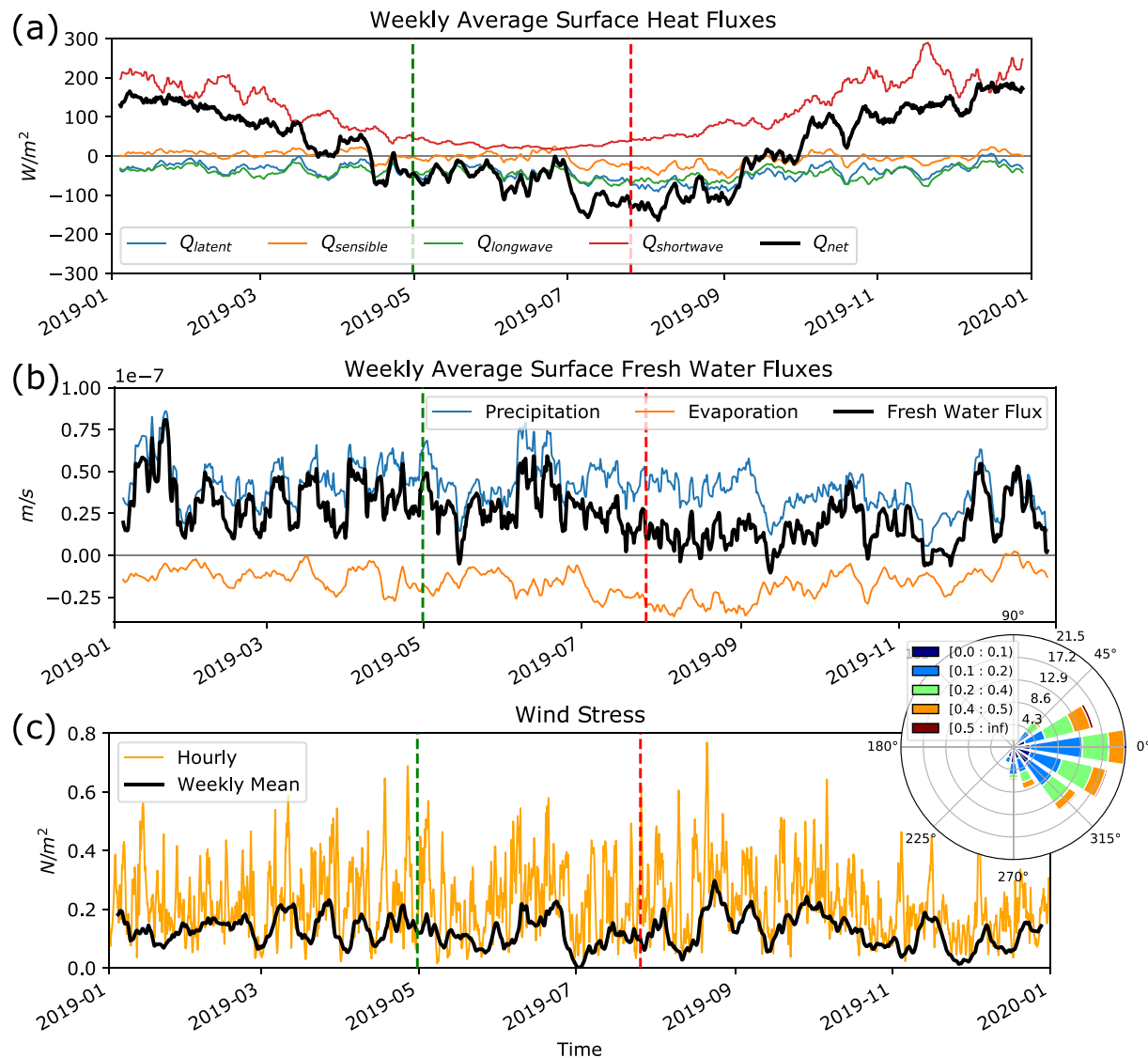


Figure 3. Surface forcing fields from ERA5. (a) Weekly averaged surface heat fluxes ($W m^{-2}$) and its components, (b) Weekly averaged surface freshwater fluxes ($m s^{-1}$), and (c) Hourly and weekly averaged surface wind stress ($N m^{-2}$). All variables were averaged spatially over 30° – $39^{\circ}E$ and 50° – $53.5^{\circ}S$. The inset (d) Shows a windrose plot of the hourly wind stress during the period of glider deployment. The direction shows wind stress orientation while the legend indicates wind stress magnitude. The dashed vertical green and red lines in each panel represent the start and end dates of the glider surveys.

surface cooling that led to a slow thickening of the mixed layer; details of the surface forcing are provided in Figure 3.

Mean hydrographic properties computed from Argo float observations (Roemmich & Gilson, 2009) and measurements from the I06S repeat transect at $30^{\circ}E$ show the dominance of the PF in setting large-scale tracer distributions in this region (Figure 4). Located at $\sim 51^{\circ}S$, the PF is associated with a region of outcropping density surfaces. In the upper 400 m of the water column, the PF acts as a barrier to mixing between warmer waters to the north and cooler waters to the south that have a temperature minimum at a depth of 150–200 m (Figure 4a). The PF also separates southern, salinity-stratified waters from temperature-stratified waters to the north (Stewart & Haine, 2016). The salinity distribution shows evidence of subduction of fresher waters along density surfaces at the core of the PF, illustrating that on large scales, this region is associated with ventilation of intermediate waters (Figure 4b). Patterns in backscatter mirror the temperature distribution, with colder waters to the south showing a local minimum in backscatter near 150 m depth and the PF marking the southern boundary of high surface backscatter values to the north (Figure 4d).

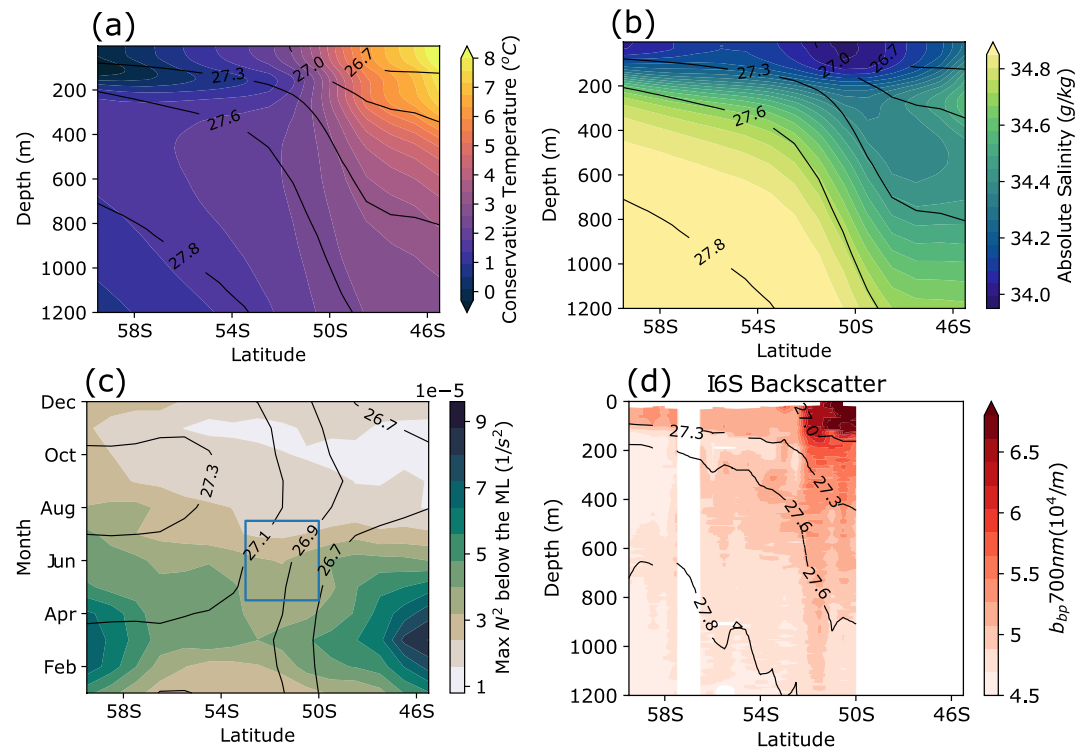


Figure 4. Hydrographic properties at 30°E. Depth versus latitude plots of (a) conservative temperature (°C) and (b) absolute salinity (g kg^{-1}) at 30°E from the Roemmich and Gilson (2009) climatological mean. (c) Hovmöller plot of the maximum N^2 observed below the base of the mixed layer (ML), with the time and meridional extent of the glider sampling shown by the blue box, also from Roemmich and Gilson (2009). (d) Depth-latitude plot of de-spiked backscatter data collected during I06S (2019); note the different latitude axis range in this panel. The σ_0 surfaces are shown as black contours, with panel (c) showing contours of surface σ_0 . White space in panel (d) denotes a lack of data.

The core of the PF is associated with a local weakening of the stratification at the base of the mixed layer, which likely enables subduction in this region (Figure 4c). Near the PF, stratification at the base of the mixed layer is strongest and the MLD itself shallowest at the end of the austral summer (March), as a result of the stratifying effects of sea ice melt and increased solar radiation (Giddy et al., 2021). During austral fall and early winter (April–July), stratification at the base of the mixed layer decreases, corresponding to a reduction in the maximum vertical stratification (Dong et al., 2008). The autonomous platforms sampled during this weakening of the stratification in austral fall, which is also consistent with the surface forcing over the deployment period (Figure 3).

3.2. High-Resolution Physical and Biogeochemical Observations

Despite their relative proximity, the distributions of temperature-salinity (θ - S) values measured by the float and by the gliders differ significantly. Throughout the deployment, the float sampled a relatively tight θ - S relationship, reflecting properties of the PF core waters (temperatures between 2°C and 2.5°C; Figure 5a). This suggests the float's trajectory was Lagrangian to good approximation, despite profiling vertically. While the gliders spent a large portion of time sampling within the PF core waters as well, they also observed water masses sourced from north of the PF (with higher SSH and temperatures warmer than 2.5°C) and from south of the PF (with lower SSH and temperatures colder than 2°C). The gliders sampled a larger range of water mass properties during the first part of the deployment, corresponding to the high-EKE region (Figure 5b). Despite our best efforts to keep the gliders close to the float during the deployment, the platforms did not sample identical water masses over the duration of the mission. In some places, this reflects the strong frontal currents and associated abrupt changes in water properties, although the platforms were geographically distant at certain times as well (Figure 2c). In fact, the gliders at times sampled

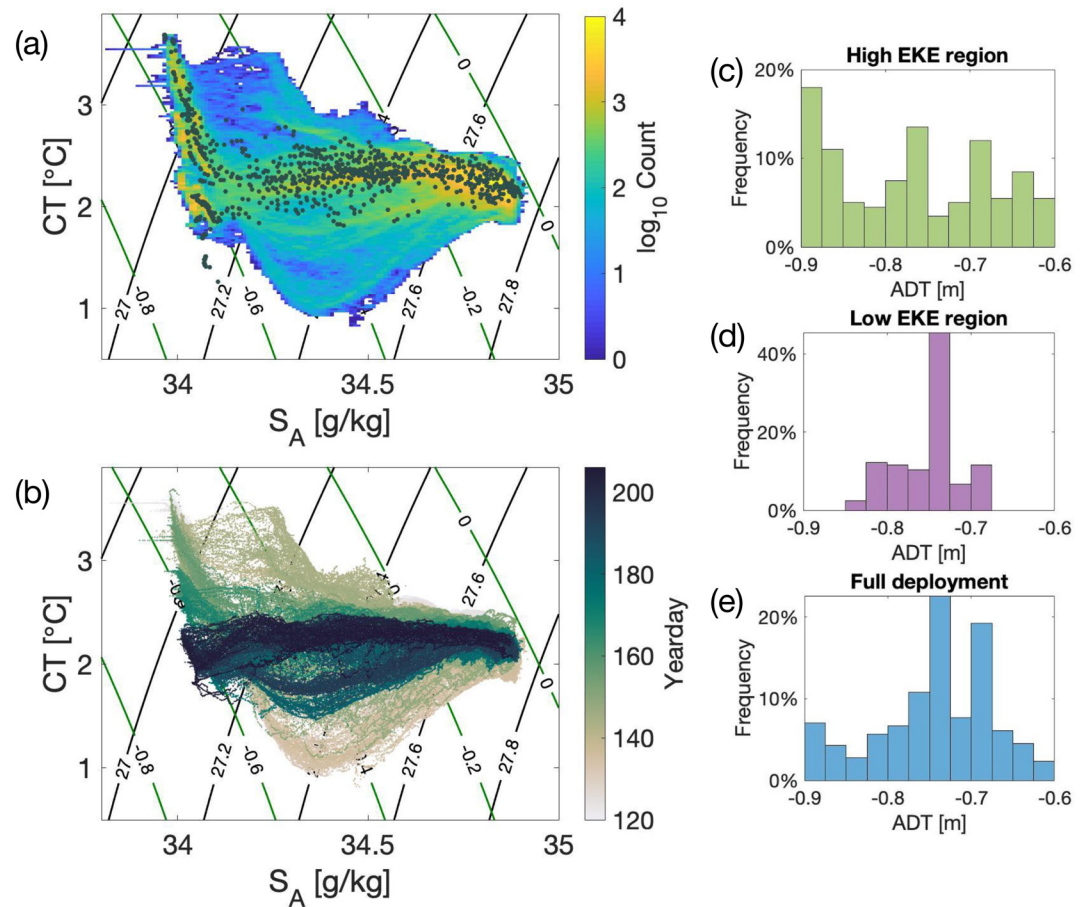


Figure 5. (a) Conservative temperature–Absolute salinity diagram for all observing platforms over the full deployment colored by the frequency of observations collected by the two gliders with given CT–SA properties, using discretizations of $\Delta T = 0.02^\circ\text{C}$ and $\Delta S = 0.01 \text{ g kg}^{-1}$. Gray points are from the Biogeochemical–Argo float during the period April 29–July 25, 2019. (b) Conservative temperature–Absolute salinity diagram colored by the yearday of the observation made by the two gliders. Black contours show potential density (kg m^{-3}) referenced to the surface, and green contours show sigma-spice (kg m^{-3}) referenced to the surface. Histograms of the absolute dynamic topography (m) (sea surface height) along the path of the gliders in (c) the high-eddy kinetic energy (EKE) region (yearday 120–155), (d) the low-EKE region (yearday 170–206), and (e) the full deployment. Made from the joint data of SG659 and SG660.

“southern-sourced” waters based on hydrographic properties despite being physically well north of the float (Figure 2b, e.g., yeardays 130–150) – a signature of lateral stirring across the PF.

Gaps in $\theta - S$ space found in the distribution of hydrographic properties are indicative of multiple small-scale fronts (Naveira Garabato et al., 2011). This frontal structure is also supported by consideration of the local SSH field along the path of the gliders. Multiple minima in the frequency distribution of SSH are indicative of the gliders sampling across more than one frontal jet (Sokolov & Rintoul, 2009; Thompson & Sallée, 2012). In the high-EKE region early in the study period, the gliders sampled across several water masses separated by multiple fronts (Figures 5b and 5c). This frontal structure is highlighted further in Figure 8a, which shows that θ – S properties are correlated with SSH in the high-EKE region. In the standing meander region, mesoscale eddies may form and enclose water properties from either side of the front (Roach et al., 2016; Thompson & Sallée, 2012). This makes it difficult to distinguish jets from eddies in the glider data, although the correlation between SSH and θ – S will primarily reveal mesoscale structure due to the resolution of the altimetry data. In contrast, in the low-EKE portion of the deployment, distinct water masses were only sampled when crossing eddies shed from the PF (Figure 5d). During this latter period, the low range of SSH values sampled, together with the quasi-Lagrangian nature of the float, suggest that the

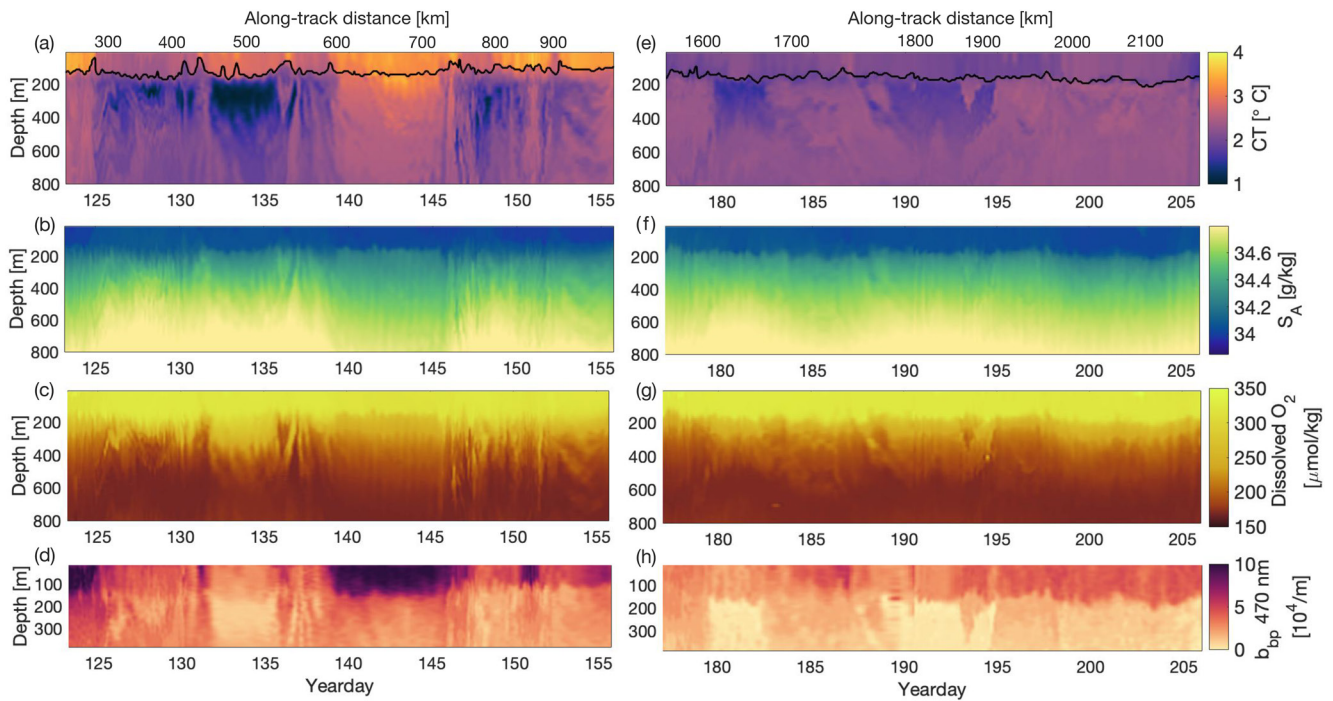


Figure 6. Glider tracer sections from SG660 in high-eddy kinetic energy (EKE) region (yeardays 125–155) showing (a) conservative temperature ($^{\circ}\text{C}$), (b) absolute salinity (g kg^{-1}), (c) dissolved oxygen ($\mu\text{mol kg}^{-1}$), and (d) backscatter at 470 nm (10^4 m^{-1}). (e)–(h) Same as in panels (a)–(d) but for low-EKE region (yeardays 177–206). Black line in panels (a) and (e) designates the mixed layer depth. Color bars apply to both left-hand and right-hand panels. Note change in depth axis for (d) and (h) compared to the other panels.

gliders and float both stay primarily within the PF core waters. Over the full deployment, the PF core waters were observed most frequently (Figure 5e).

The similarities and differences in tracer variability between the high-EKE and low-EKE regions is further illustrated by the representative depth-time series plots of physical and biogeochemical properties from one of the gliders (SG660) shown in Figures 6 and 7. Periods dominated by mesoscale variability are characterized by homogeneous properties in the upper 500 m of the water column as well as curvature in the isopycnals that is anti-correlated with SSH, for example, during yeardays 140–145 (Figures 6a, 7a and 7b). Correlated variations between the vertical displacement of isopycnals and SSH are not observed to the same extent in the low-EKE regime, although the signature of a mesoscale eddy is present in the tracer observations collected between days 187 and 194 (Figures 6e–6h). Higher frequency and finer scale variability also occurs at the typical glider sampling scale, $O(<1 \text{ day}, <10 \text{ km})$, throughout the time series. This sub-mesoscale variability is enhanced along the periphery of the mesoscale structures, consistent with increased strain in these regions (Brannigan, 2016; Siegelman, 2020). These features are particularly noticeable in temperature (Figures 6a and 6e), which acts as a passive tracer below the mixed layer, as well as in oxygen and optical backscatter (Figures 6c, 6d, 6g and 6h). Outside of the coherent mesoscale features, in what is sometimes referred to as the “submesoscale soup” (McWilliams, 2016), fine-scale tracer variability appears as horizontal layers, primarily in the high-EKE region (Figures 6a, 6c, 6e and 6g). Notably, the MLD is more variable in the high-EKE region, shoaling particularly at the edges of mesoscale eddies, and then stays relatively constant in the low-EKE region (black line in Figures 6a and 6b).

The optical backscatter distribution is closely correlated with temperature, with warmer temperatures associated with higher backscatter values (Figures 6d and 6h, 470 nm wavelength; sections of the 700 nm backscatter are similar but not shown). The temperature-backscatter relationship is consistent with the large-scale distribution observed during the I06S cruise (Figure 4d), suggesting that in both of these properties, stirring cascades variance to smaller scales. A compelling feature of both the temperature and backscatter data is the nonmonotonic vertical distribution, with the presence of prominent low anomalies located just below the mixed layer in the high-EKE region, sandwiched between higher values above and below

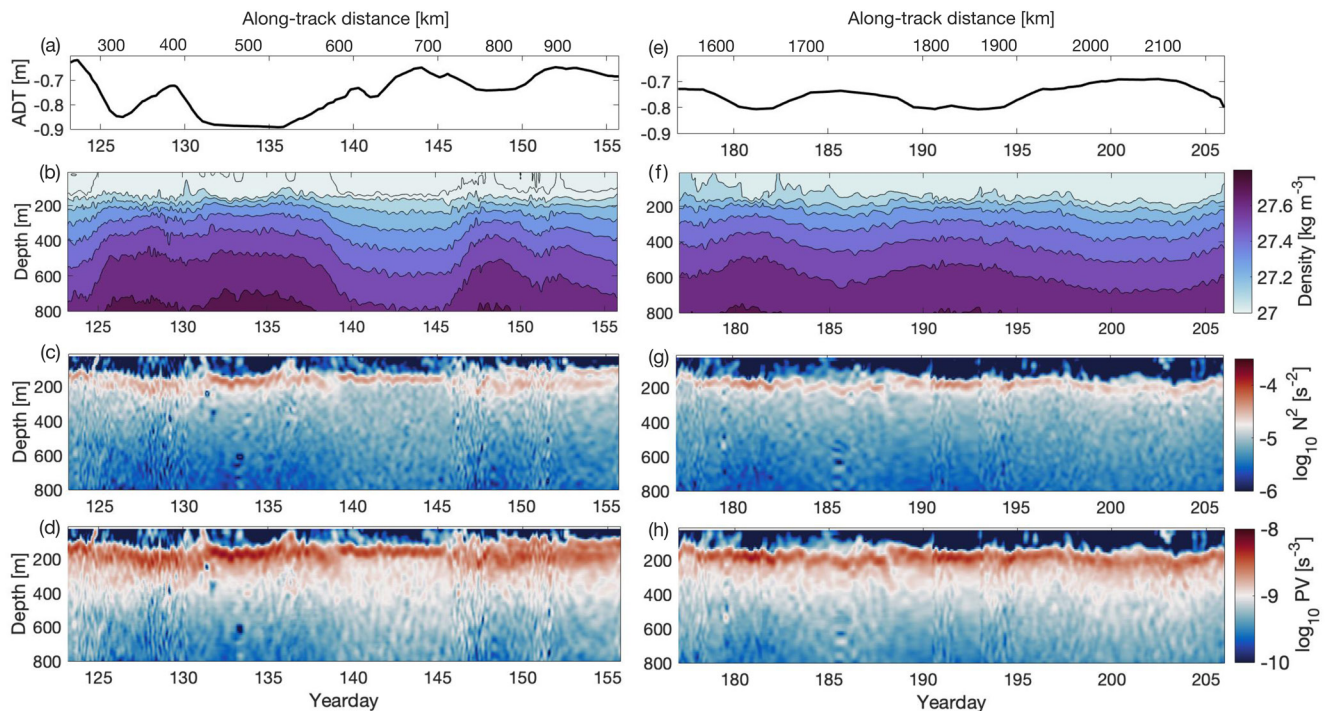


Figure 7. Glider derived tracer sections from SG660 in high-eddy kinetic energy (EKE) region (yeardays 125–155) showing (a) absolute dynamic topography (m), (b) potential density (kg m^{-3}), (c) vertical buoyancy gradient, N^2 (s^{-2}), and (d) Ertel Potential Vorticity (PV) (s^{-3}). (e)–(h) Same as in panels (a)–(d) but for low-EKE region (yeardays 177–206). Color bars apply to both left-hand and right-hand panels.

(yeardays 127–132 and yeardays 145–150, between 150 and 250 m). The temperature minima could be explained as a remnant of cold Winter Water that is capped in the summer by a warmer surface layer. In contrast, the backscatter minima must arise from lateral or along-isopycnal advection. For instance, this feature could arise from the subduction of cold surface waters with low backscatter sourced from south of the PF. Notably, the backscatter minima at the base of the mixed layer (at approximately 150 m) only occurs in the high-EKE region, even though in the downstream region backscatter has a similar correlation with temperature at mesoscales (see mesoscale features over yeardays 132–135 and 187–195).

There is generally strong stratification at the base of the mixed layer throughout the deployment, which may limit exchange between the surface boundary layer and the ocean interior (Figures 7c and 7g). However, in the high-EKE region, the glider encountered intermittent periods of weakened upper ocean stratification collocated with the edge of strong mesoscale features. Although there is little evidence for coherent boluses of weakly stratified, low PV waters in the interior, high PV waters with strong stratification are observed to intrude into the mixed layer in the high-EKE region (e.g., yeardays 125, 132, and 136; Figures 7d and 7h). The advection of high PV waters toward the surface is reminiscent of the tracer distributions associated with upwelling induced by anticyclonic eddies in the model-based study of Brannigan (2016) (their Figure 2).

The complicated 3D circulation that the gliders sampled along their trajectories motivates a consideration of biogeochemical distributions in temperature-salinity space as well as geographic space. Optical backscatter distributions, despite the intricate variations along the gliders' trajectories (Figures 6d and 6h), are largely shaped by the frontal structure in this region, with elevated backscatter values found north of and in the core of the PF and considerably lower backscatter values to the south (Figure 8c). Regions with high surface backscatter values do not all have the same vertical distributions; backscatter values are elevated to much greater depths and density classes for those waters associated with the core of the PF (Figures 8c and 8d). This suggests that subduction of water with high backscatter values (and potentially high POC) is linked to specific water masses and water mass formation processes.

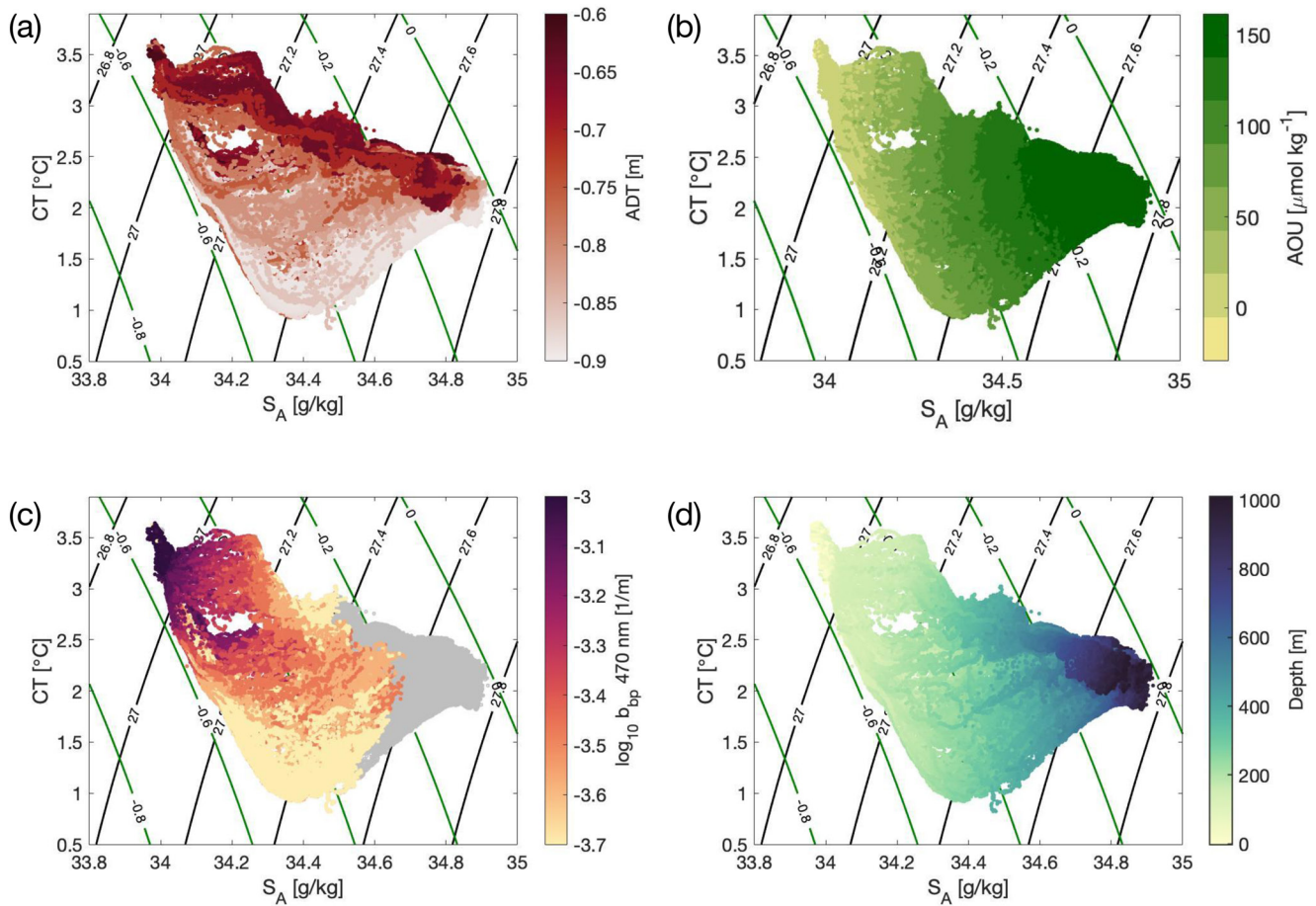


Figure 8. Distribution of physical and biogeochemical properties in temperature-salinity space from the standing meander region (yeardays 120–155). The points are colored with the following properties: (a) Absolute dynamic topography (SSH) (m) for each glider profile, (b) apparent oxygen utilization (AOU) ($\mu\text{ mol kg}^{-1}$), (c) $\log_{10} b_{bp}$ at 470 nm (m^{-1}), and (d) depth (m). Gray points in the backscatter plot represent data between 400 and 1,000 m where temperature, salinity, and oxygen measurements were collected but biogeochemical properties were not. In all panels, black contours show potential density (kg m^{-3}) referenced to the surface, and green contours show spice (kg m^{-3}) referenced to the surface. Made from the joint data of SG659 and SG660.

The distribution of AOU also shows distinct behaviors between the different frontal regions. South of the PF core waters, contours of AOU (in temperature-salinity space) are predominantly aligned with contours of spice (Figure 8b). The resulting gradient of AOU on density surfaces may arise from lateral advection as cold anomalies are correlated with low AOU/high dissolved oxygen anomalies. This suggests that these waters have recently been subducted to the south of the study region, since these density classes do not access the mixed layer in the float/glider observations. North of and within the PF core waters, contours of AOU are largely aligned with density contours, such that AOU increases with depth and density. Those density surfaces with low AOU anomalies south of the PF have higher AOU values north of the PF, suggesting that recently ventilated waters are localized to the PF.

3.3. Submesoscale Structures

Submesoscale motions are typically enhanced in the ocean surface boundary layer due to reduced stratification and the potential for frontogenesis (McWilliams, 2016; Thomas et al., 2008). Characterization of mixed-layer frontal structure has been a common method for assessing the potential for submesoscale motions and instabilities (Thompson et al., 2016), with previous studies showing that the statistical properties of the mixed layer can change over relatively short spatial scales (Viglione et al., 2018). In the SOGOS glider data, strong lateral buoyancy gradients in the along-track direction form in the mixed layer in the high-EKE region, as disparate water masses are stirred together (Figure 9). Both temperature and salinity anomalies

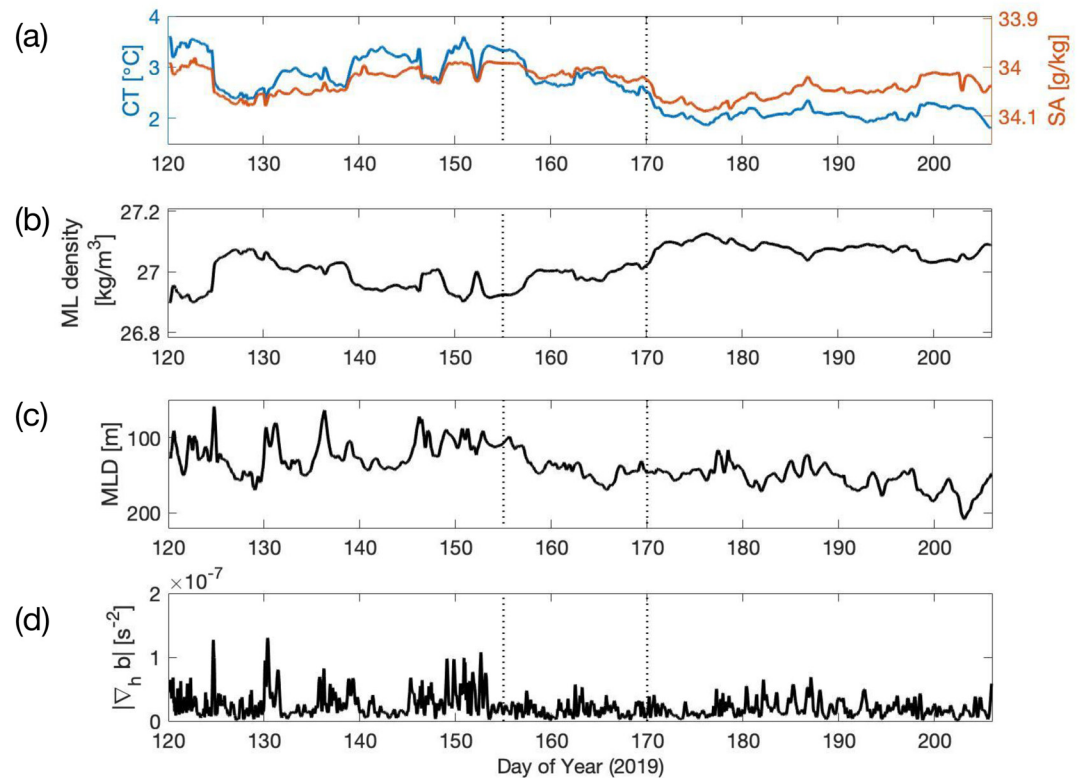


Figure 9. (a) Mixed layer temperature (blue line) and salinity (red line) variations throughout the glider time series. The vertical axes are scaled by α (temperature) and β (salinity) so that variations in CT and S_A have equal effects on density. (b) Mixed layer density (kg m^{-3}). Vertical axis has been scaled to the minimum and maximum contributions by the temperature and salinity presented in panel (a). (c) mixed layer depths as defined by a density difference criteria of 0.05 kg m^{-3} from a 10-m reference level. (d) Horizontal gradient of buoyancy in the mixed layer. Dotted line at yearday 155 denotes an end to the high-eddy kinetic energy (EKE) region and the dotted line at yearday 170 denotes the start of the low-EKE region. Data from SG660.

in the surface layer work in concert to enhance the buoyancy anomalies. The compounding contributions from temperature and salinity intensify lateral buoyancy gradients when these water masses are stirred by mesoscale eddies (for example, on yeardays 124, 139, 146, and 149; Figure 9b). Lateral buoyancy gradients have peak magnitudes and are most variable during the initial month of the deployment (Figure 9d). Strong surface buoyancy gradients are collocated with the edge of coherent mesoscale eddies or small-scale fronts, which are commonly associated with an intermittent shoaling of the mixed layer on the time scale of 1–2 glider dives ($\approx 3\text{--}10 \text{ h}$). The magnitude of the mixed-layer lateral buoyancy gradient weakens over the duration of the deployment (Figure 9d). This weakening could be caused by seasonal-scale changes in surface forcing (Figure 3a); however, the fact that the MLD remains relatively uniform (Figure 9c) suggests that it is more likely related to the reduction in vigorous stirring by mesoscale motions later in the deployment.

The prevailing paradigm for ventilation of the surface mixed layer by submesoscale motions has been along-isopycnal subduction at fronts, moving water masses across the base of the mixed layer (Freilich & Mahadevan, 2019; Omand et al., 2015; Ruiz et al., 2009). This view has been supported by consideration of tracer distributions in density space, in which tracer anomalies tend to be aligned along isopycnals, even if they have a significant vertical structure (see Figure 3 in Lévy et al., 2018, for instance). In the glider observations, there are significant variations in spice and AOU along density surfaces, and anomalies are also often coherent across a broad range of densities, particularly below the mixed layer (Figure 10). The lack of obvious, coherent along-isopycnal subduction events indicates that other processes are active or that the subduction features occur at small scales so that gliders only observe them intermittently. Consistent with Figure 8b, AOU and spice anomalies are tightly correlated in regions associated with cold, southern-sourced waters. Anomalies in both spice and AOU echo the signatures of mesoscale features seen in Figures 6 and 7.

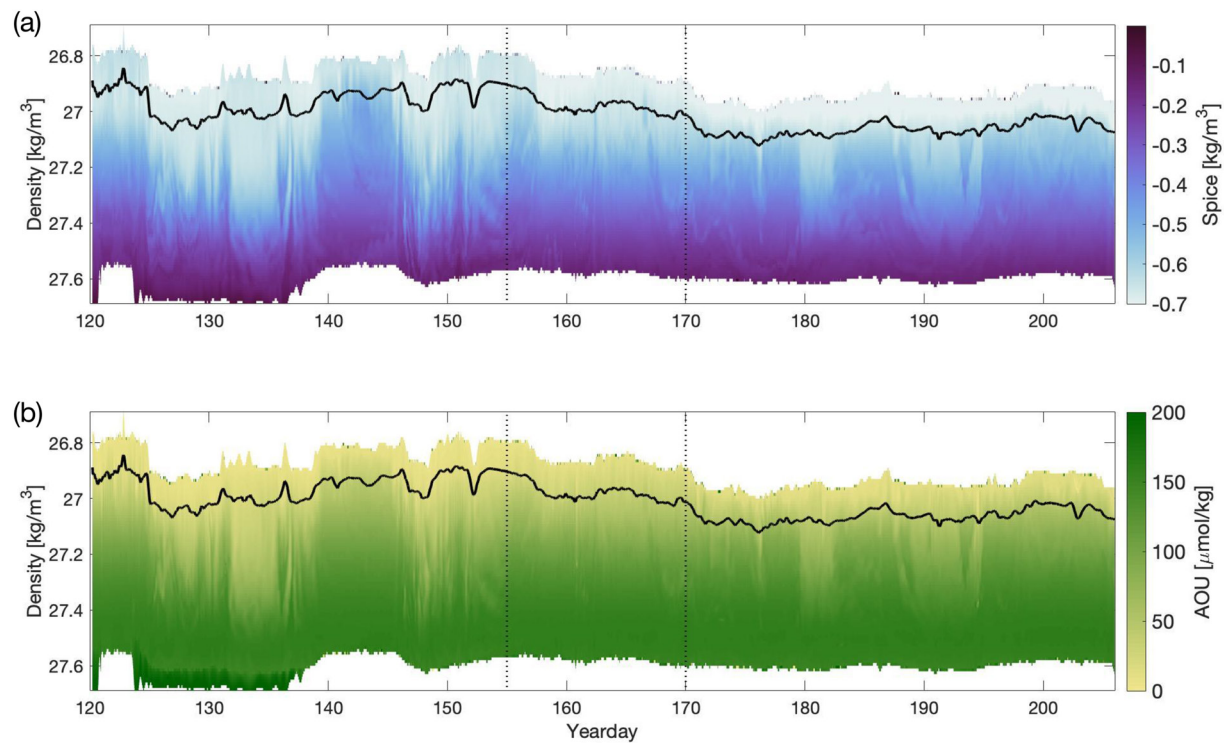


Figure 10. Time series of (a) spice (kg m^{-3}) and (b) apparent oxygen utilization (AOU) ($\mu\text{mol kg}^{-1}$) from glider SG660 mapped on to potential density surfaces. Black line denotes the position of the mixed layer base. Dotted line at yearday 155 denotes an end to the high-eddy kinetic energy (EKE) region and the dotted line at yearday 170 denotes the start of the low-EKE region. Data from SG660.

At eddy peripheries or between eddies, most noticeable where there is a strong tilting of density surfaces (e.g., day 124 or 140), there are enhanced submesoscale variations (Siegelman, 2020). In these regions, both spice and AOU anomalies are coherent across a broad range of densities, even well below the base of the mixed layer, which suggests that stirring by (largely barotropic) eddies is likely the primary mechanism for generating this structure. Smaller-scale variations on density surfaces exist primarily in the high-EKE region, suggesting that in this region, deep density classes are accessed by filamentary structures that transport tracers vertically.

Although tracer anomalies are not predominantly aligned with density surfaces, the signature of surface mixed layer-interior exchange is apparent nonetheless. In several locations throughout the deployment, low AOU (recently ventilated) waters intrude well below the MLD (Figure 10). Most notably, between yeardays 148–152, recently ventilated waters reach density surfaces typically associated with Upper Circumpolar Deep Water ($>27.6 \text{ kg/m}^3$). In addition to the observations of low spice and low AOU waters extending to denser isopycnals, there is also evidence of deep, oxygen-depleted (high AOU) waters reaching across the base of the mixed layer (yearday 140), consistent with high-stratification waters intruding into the mixed layer at eddy peripheries in Figure 7c.

3.4. Biological Signatures

While we have thus far focused on physical processes that generate the variability observed in both physical and biogeochemical tracer distributions, biological variability was also apparent in the glider and float data. Spikes in backscatter can be signatures of aggregated particulates (Briggs et al., 2011, 2020). Typically the export of aggregates is dominated by gravitational sinking, rather than by active advective processes that contribute to the export of smaller particles (Boyd et al., 2019). The number of aggregated particles, counted by large spikes in the b_{bp} , is variable across the deployment but is often correlated with the concentration of backscatter in the mixed layer, consistent with the export process for large particulate aggregates being primarily one-dimensional (Figures 11a and 11b). The regions of highest backscatter at the surface are

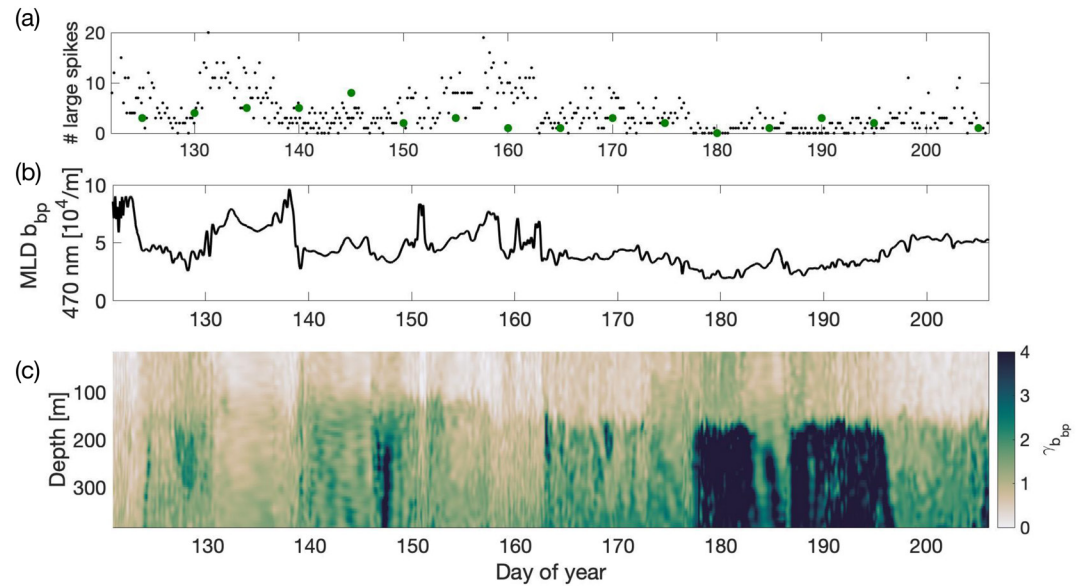


Figure 11. (a) Black dots: number of large spikes in 470 nm backscatter below the mixed layer per each downcast and upcast of SG659. Green dots: number of large spikes in 700 nm backscatter in Biogeochemical-Argo float data from WMO 5906030. Note that only qualitative patterns should be considered as the sampling rates of the gliders and float were not the same. (b) 470 nm backscatter in the mixed layer from SG659. (c) Backscatter spectral slope ($\gamma_{b_{bp}}$) from SG659. Figure made with SG659 due to potential errors in the 700 nm backscatter data from SG660.

correlated with warmer waters sourced north of the PF (e.g., yeardays 120–122 and 130–140). While large aggregates may sink out of the water column, smaller non-aggregated particulate matter may be transported along isopycnals to intermediate depths (Dever et al., 2021), a process that highlights the impact of 3D transport on tracer distributions.

The float backscatter data, which were collected to greater depth than that collected by the gliders, reveal that enhanced backscatter can exist at depths down to 600 m in the high-EKE region (not shown). Although the platforms did not follow identical pathways and backscatter processing between the platforms differ, the distribution of spikes in 700 nm backscatter from float WMO 5906030 is qualitatively similar to that determined from the gliders (Figure 11a). However, due to the 5-days sampling period of the float, the small-scale structure within the patterns in the glider backscatter spike data is absent in the float backscatter data, which can have a significant impact on longer-term mean values. Observing platforms that rely on sampling on the order of many days will miss this high-frequency variability, which provides information on particulate export from the surface ocean, especially due to submesoscale dynamics.

Backscatter spectral slope ($\gamma_{b_{bp}}$), which was calculated using two wavelengths of despiked backscatter from $bbp(\lambda) = bbp(\lambda_0) \frac{\lambda}{\lambda_0} - \gamma_{b_{bp}}$, has been shown to reflect the size distribution of suspended particles (Dever et al., 2021; Kostadinov et al., 2009). Qualitatively, the spectrum of backscatter will flatten as the percentage of larger particles increases; a transition from large to small $\gamma_{b_{bp}}$ may thus indicate a transition into a more productive region with larger phytoplankton. Estimates from satellite observations of $\gamma_{b_{bp}}$ in the surface ocean of the Southern Ocean suggest values of 0.5–1.5 (Loisel et al., 2006), consistent with our glider estimates.

Ranging from 0 to 4, $\gamma_{b_{bp}}$ is generally low in the surface mixed layer (Figure 11c), suggesting a greater proportion of large-sized particles that are potentially diatoms, the dominant marine primary producers in the Southern Ocean (de Baar et al., 1999; Rousseaux & Gregg, 2014). Below the mixed layer, $\gamma_{b_{bp}}$ increases, particularly in regions where backscatter concentrations are low (e.g., yeardays 146–147, 178–196); here a larger proportion of small-sized particles are likely dominating the backscatter measurements. In general,

the high-EKE region has a weaker vertical gradient in γ_{bhp} across the base of the mixed layer, suggestive of enhanced surface-interior exchange.

The particle composition distribution suggests plankton communities with differing compositions are intricately mixed in this localized region of high EKE in the Southern Ocean. The PF typically acts as a barrier to mixing of biological communities and is a known front in silicate, which has implications for the growth of diatoms (Freeman et al., 2018). However, the high EKE at standing meanders may allow plankton communities to be stirred into proximity and ultimately to mix. While these communities remain intact when transported within coherent mesoscale features (e.g., days 178–196 in Figure 11c), mixing of these communities occurs in filaments at the edges of eddies. Such mixing is especially prevalent in the high-EKE region, implying a regional hotspot for community mixing both in the surface ocean and at depth (Figure 11c).

4. Discussion

4.1. Cross-Scale Contributions to Variability

Our understanding of the role of mesoscale and submesoscale processes in setting the distribution of biogeochemical tracers has been shaped by observations of organic matter subduction (Mahadevan, 2016; Stukel & Ducklow, 2017), as well as heavily instrumented studies that tracked the transport of tracer anomalies between the surface ocean and the interior (Omand et al., 2015; Stukel et al., 2017). However, open questions remain about the relative contributions that processes at different scales make to setting these patterns. This is particularly true in the Southern Ocean where observational surveys that resolve submesoscale features have been rare (Adams et al., 2017), and geographic regions or features that enhance export via small-scale subduction remain relatively unexplored.

Stirring by mesoscale eddies is known to produce filaments and anomalies of spice, AOU, and biogeochemical tracers at smaller submesoscales, particularly in regions where water masses with differing formation processes and community compositions are adjacent (Balwada et al., 2018, 2020; Smith & Ferrari, 2009). In the Southern Ocean, the PF supports large gradients in temperature and salinity that, via stirring by geostrophic turbulence, can produce a direct cascade of tracer variance to small scales, especially below the mixed layer. Indeed, the largest variance of tracers occurs on density surfaces below the mixed layer and can be explained primarily by stirring of large-scale gradients at the mesoscale, particularly within the high-EKE standing meander region (Figures 8 and 12). Furthermore, the majority of the observed tracer features at the submesoscale are not aligned along density surfaces. Thus, vigorous stirring along tilted density surfaces, ubiquitous in the Southern Ocean and particularly at the PF, must be critical in assisting with the export of biologically relevant tracers from the surface layer to the interior. To this end, parameterizations that assume purely vertical sinking for particulate matter may misrepresent the subduction of organic matter in the Southern Ocean, particularly due to the 3D structure of high EKE and enhanced stirring.

Yet, these observations also provide evidence that submesoscale motions are likely impacting surface boundary layer-interior exchange. This is particularly true for waters sourced from north of the PF, for which tracers such as AOU are more aligned with density surfaces (Figure 8b). Furthermore, high AOU and spice anomalies that reach across the base of the mixed layer occur almost exclusively along the periphery of coherent mesoscale features, as distinguished by co-variations in SSH and density surfaces. More broadly, stirring along density surfaces may also generate strong vertical gradients across the base of the mixed layer that then increase tracer fluxes due to turbulent vertical mixing at the submesoscale. Observations with high spatial and temporal resolution, sampled in a way that crosses submesoscale fronts at a near-perpendicular angle, are necessary for inferring ageostrophic vertical velocity w from existing parameterizations. While we were not able to provide a direct estimate of w with this data set, there is strong evidence that upper-ocean submesoscale motions are playing a role in the subduction of surface waters, in a compact region in the lee of topography. Our observations thus allow for the validation of models that predict enhanced vertical tracer exchange where submesoscale dynamics are active. Ultimately, because features at the submesoscale are shaped by the mesoscale, the coupling of these scales plays an important role in shaping the tracer gradient, with submesoscales having a more prominent role in enabling exchange across the base of the mixed layer and mesoscales shaping tracer distributions at depth.

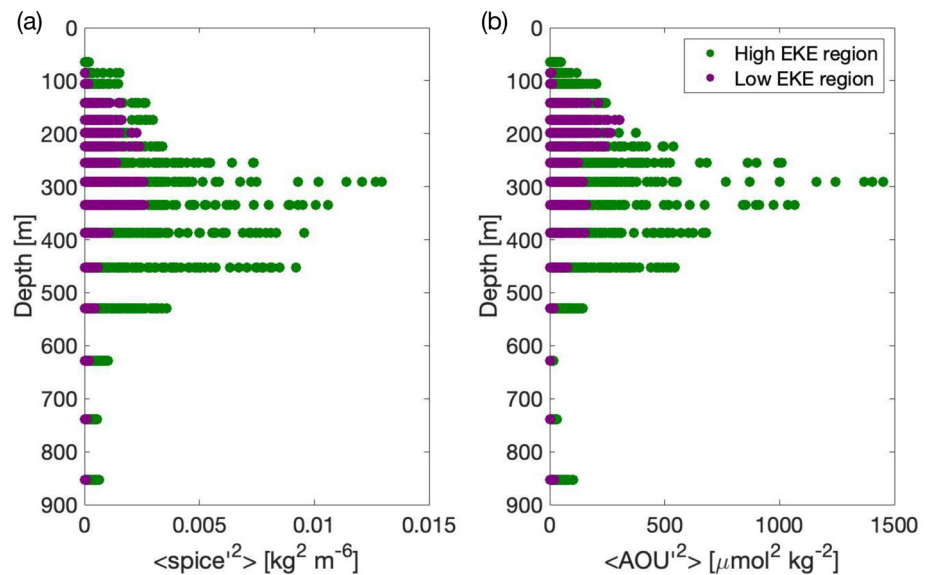


Figure 12. (a) Squared anomalies of spice in the high-eddy kinetic energy (EKE) (green) and low-EKE (purple) regions on isopycnals, plotted on the average depth of each isopycnal. (b) Same as in (a) but for apparent oxygen utilization (AOU). Individual points are the squared difference of spice (or AOU) at a point and the running mean (50 km) of spice (or AOU) along the isopycnal. Joint data of SG659 and SG660.

Isolating physical mechanisms responsible for tracer distributions becomes challenging when constrained solely by vertical profiles from floats that sample every $O(10)$ days. Higher-resolution glider measurements, which sample scales of $O(\text{hours}, 1 \text{ km})$, provide greater insight into anomalies resulting from mesoscale stirring and active submesoscale processes, which may be either misclassified or entirely absent in typical float profiles. Figure 13 shows how the BGC-Argo float and the gliders sampled around the edge of a mesoscale eddy in the low-EKE region of the deployment. The quasi-Lagrangian float was advected cyclonically

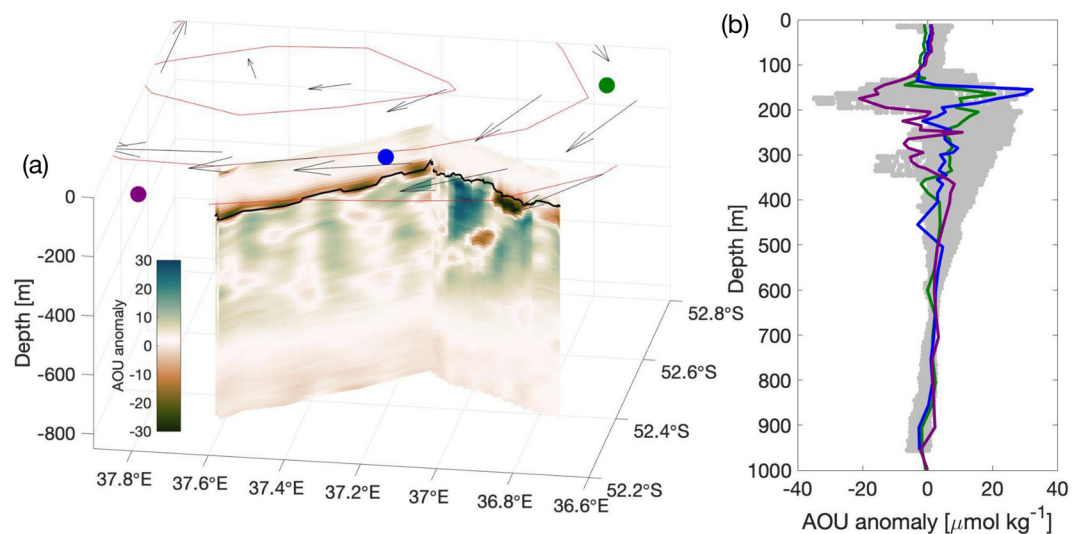


Figure 13. Apparent oxygen utilization (AOU) anomalies in glider and float data in a mesoscale eddy. (a) Curtain figure of the AOU anomaly from the mean value at each depth from SG660 between year days 187 and 193. MLD is plotted as a black line. Sea level anomaly from day 190 is given by the red contours; the arrows show the geostrophic velocity with peak speed of (20 cm s^{-1}) . Green, blue, and purple lines represent the locations of vertical profiles done by the Biogeochemical-Argo float on year days 185, 190, and 195, respectively. (b) AOU anomaly with depth for the glider (gray) and each of the 3 float profiles with the same colors as in panel (a). Note the float did every other profile to 2,000 m but only the upper 1,000 m are shown.

around the edge of the eddy, performing three purely vertical profiles. In contrast, the glider sampled across the edge of the eddy and crossed through a coherent, low-AOU anomaly that extended below the mixed layer to a depth of 400 m, likely indicative of waters recently subducted from the surface layer (Figure 13a). The feature was not clearly observed by the float although the instruments were all within 20 km of each other (Figures 2c and 13b). In fact, both gliders crossed the mesoscale eddy edge, but only one observed the submesoscale subduction feature, highlighting the azimuthal variability around a given eddy. Llorca et al. (2018) showed that, in high-EKE regions of the Southern Ocean, anomalies of spice and AOU at depth are regularly present in BGC-Argo float profiles and described a method to attribute such anomalies to submesoscale dynamics. Our data illustrate that an accurate interpretation of profiling float observations must account for the fact that small numbers of floats will not capture the full signature of the submesoscale, particularly because these instruments do not often cross eddy edges. To this end, parameterizations that assume purely vertical sinking for particulate matter may misrepresent the subduction of organic matter in the Southern Ocean, particularly due to the 3D structure of high EKE and enhanced stirring.

4.2. The Case for Southern Ocean Ventilation Hotspots

Standing meanders of the Southern Ocean, characterized by high EKE and rates of strain, may play an outsized role in the export of organic matter due to their ability to sustain a persistent and vigorous mesoscale eddy field that provides a source of frontogenesis and catalyzes strong submesoscale motions that enhance vertical velocities and fluxes (Siegelman, 2020). Our data set is unique in that the gliders and float sampled regions of both strong and weak mesoscale strain, corresponding roughly to the first and second halves of the deployment, respectively (Figure 2a). Evidence for subduction at the submesoscale is greater in the high-EKE portion of our study region, where larger lateral buoyancy gradients, stronger tracer variability, and high oxygen values penetrating deeper into the water column are all diagnostics consistent with enhanced submesoscale activity (Figures 9 and 10). The MLD is both shallower on average and more variable in the high-EKE region (Figure 9), potentially demonstrative of shoaling as a result of mixed layer instability (du Plessis et al., 2017; Thompson et al., 2016; Viglione et al., 2018). This observation is also consistent with numerical models, such as Balwada et al. (2018), that find that mixed layers are shallower downstream of a topographic feature where an active submesoscale field is present. Finally, the deepest penetration of the backscatter data away from the surface is found within the core of the PF, associated with the strongest frontal structure (Figure 8c).

Further evidence for localized ventilation in the standing meander is the stronger along-isopycnal tracer variance in the high-EKE region directly in the lee of topography than in the low-EKE region downstream (Figure 12). The difference in tracer variance between the high- and low-EKE regions is particularly apparent on isopycnals with average depths of 250–500 m. At times these isopycnals reach close to the base of the mixed layer, and thus this variance can influence the exchange of tracers between the interior ocean and the surface layer. The peak in variance is deeper in the high-EKE region (350 m) compared to the low-EKE region (250 m). In contrast to these mid-depth isopycnals, anomalies are low on isopycnals found in the surface ocean because of the homogenizing nature of the mixed layer (the average MLD is 140 m). These tracer variance characteristics suggest that vigorous stirring by coherent eddies within the standing meander plays a dominant role in setting tracer distributions and gradients in the interior ocean. Furthermore, the peak in tracer variance occurs at greater depths in the high-EKE region as compared to downstream, despite deeper mixed layers in the latter (Figure 12). While much of the tracer variance generation likely occurs through mesoscale stirring, injection of anomalously low AOU, low spice waters from the surface is required to maintain the range of observed tracers.

While small-scale fluctuations in the stratification at the base of the mixed layer are observed by the glider (Figures 7c and 7g), overall there is only a slight difference in the maximum value of stratification (N_{max}^2) between the high-EKE standing meander and the low-EKE downstream region. In the high-EKE region, both N_{max}^2 (Figure 14a) and lateral buoyancy gradients in the mixed layer (Figure 14b) are slightly stronger, but by less than a factor of 2. In contrast, substantial changes are found in the vertical tracer gradient across the base of the mixed layer (shown as a change in spice in the 10 m above and below the depth of N_{max}^2 in Figure 14), with gradients within the high-EKE region reduced by almost an order of magnitude as compared to those in the low-EKE region. Weaker vertical gradients in tracers suggest that those waters were

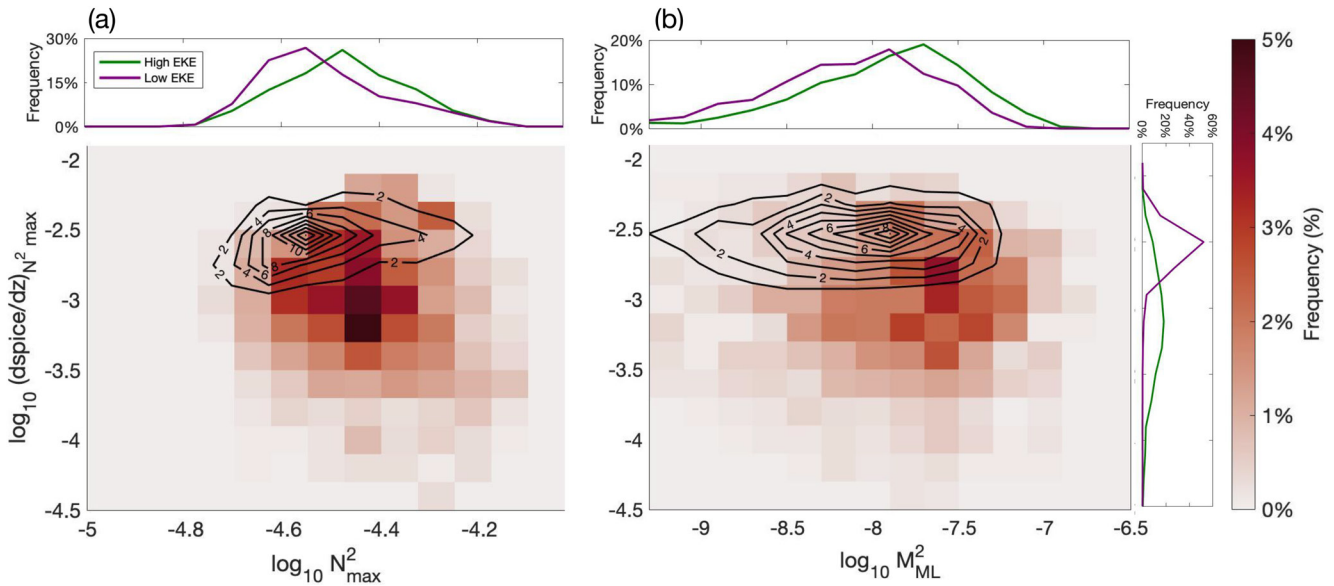


Figure 14. Joint probability distribution functions of (a) \log_{10} maximum vertical gradient of buoyancy (N_{max}^2), and (b) \log_{10} horizontal gradient of buoyancy in the mixed layer (M_{ML}^2) and with the \log_{10} of the absolute value of vertical spice gradient at the depth of N_{max}^2 . Colors show the distribution for the high-eddy kinetic energy (EKE) region; contours give that for the low-EKE region. Values of the joint probability for the contours for the low-EKE region are labeled. The one-dimensional histograms show the probability distribution of (a) $\log_{10} N_{max}^2$ and (b) $\log_{10} M_{ML}^2$ for the high-EKE region (green) and low-EKE region (purple). Made from the joint data of SG659 and SG660. Discretization: $\Delta N^2 = 0.075$, $\Delta M^2 = 0.2$, $ds_{spice}/dz = 0.2$.

recently subducted below the mixed layer. While gradients of spice can possibly be impacted by seasonal or meridional changes, the signal of reduced vertical tracer gradients is also robust in AOU, which has a relatively constant value near the surface. Waters between the depth of N_{max}^2 and the depth of $N_{max}^2 + 200$ m in the high-EKE region are substantially more likely to have lower values of AOU than those in the low-EKE region, suggesting these waters have been more recently ventilated and subducted below the depth of high stratification, potentially via active submesoscale processes (Figure 15). Whether this alignment of increased ventilation with higher EKE is a pattern that holds across the Southern Ocean remains an interesting open question.

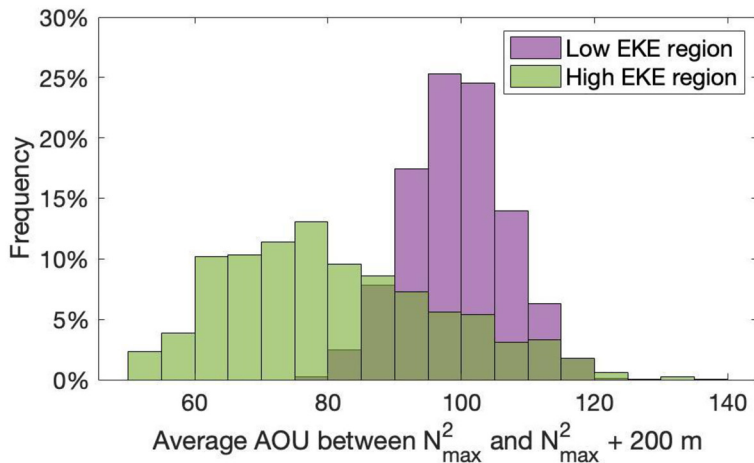


Figure 15. Probability distribution of the average value of AOU ($\mu\text{mol kg}^{-1}$) between the depth of N_{max}^2 and the depth of $N_{max}^2 + 200$ m. Green bars represent the high-eddy kinetic energy (EKE) region and purple bars the low-EKE region. Made from the joint data of SG659 and SG660.

In this data set, there is only weak evidence for the subduction of low PV (weak stratification) anomalies into the interior. This can be contrasted with the intense surface boundary layer-interior exchange that has been observed in the wintertime North Atlantic (Thompson et al., 2016). This characteristic of the SOGOS data differs from a recent study by Bachman and Klocker (2020), in which an extremely high-resolution simulation ($1^\circ/120^\circ$) was employed to argue that topographically steered jets produce localized regions of enhanced ventilation. These simulations, focused on the region around the Kerguelen Plateau, produced a strong stationary jet north of the plateau, with surface velocities and EKE variations similar to our study region. Focusing on the topographically steered jet, Bachman and Klocker (2020) suggested that a westerly wind stress can produce a destabilizing Ekman buoyancy flux that generates convective mixing and intense exchange with the interior (Thomas & Lee, 2005). Most diagnostics in this study do not extend into the standing meander region just downstream of the plateau. While we can't rule out the possibility that a similar mechanism occurs as the PF passes directly over the SWIR, the float and the gliders all measure stratification levels at the base of the mixed layer that are much greater than one would expect if convective mixing was active. Our observations suggest instead that ventilation peaks as the jet becomes more variable and filamented in the lee of topography and mesoscale stirring intensifies.

Considering the SOGOS observations in the context of our current understanding of the Southern Ocean, a picture emerges where instabilities associated with topographically steered jets give rise to an energetic field of mesoscale eddies. The jet itself has enhanced gradients in tracer properties that are then effectively stirred in the standing meander. This stirring strengthens horizontal surface buoyancy gradients, leading to an active submesoscale velocity field. The depth to which these submesoscale motions penetrate is difficult to determine from our observations but likely depends strongly on the stratification at the base of the mixed layer. During our study period, this stratification appears to be relatively strong due to the influx of freshwater and low mean wind stress. Intermittent, strong wind events ($>0.5^\circ\text{N m}^{-2}$) did occur several times over the glider deployment (Figure 3c), which may have acted to destabilize the mixed layer, similar to the results of Bachman and Klocker (2020) or Giddy et al. (2021). However, even if the submesoscale tracer fluxes are localized to the surface ocean, they still provide a continuous source of recently ventilated surface waters that are effectively stirred by the mesoscale, generating fine-scale gradients along density surfaces. Thus, through a combination of mesoscale stirring and submesoscale fluxes in the surface boundary layer, exchange between the surface ocean and the interior may be enhanced.

Observations such as those described here, together with model simulations, have suggested that standing meanders in the ACC may play an outsized role in air-sea exchange as well as tracer exchange between the surface and interior ocean. Process studies have demonstrated that this exchange is dependent on dynamics at the mesoscale and submesoscale and that along-stream variability created by standing meanders can result in vital regions of subduction and ventilation. Enhanced vertical velocities and vigorous stirring result in increased tracer variability that can lead to highly localized ventilation of old waters; in turn, localized ventilation impacts air-sea fluxes due to a disequilibrium between the atmosphere and surface ocean carbon dioxide (pCO_2) concentrations. Year-round data from BGC-Argo floats have allowed for further investigation into the locations of carbon uptake and outgassing in the ACC. These float-based estimates show that the regions around the Polar Front exhibit significant outgassing during autumn and winter, likely associated with the large-scale upwelling of old, carbon-rich waters (Gray et al., 2018). The development and deployment of unmanned surface vehicles has further expanded the collection of ΔpCO_2 concentrations across the atmosphere and surface ocean (Sutton et al., 2021). However, the role of localized regions of enhanced EKE has not yet been diagnosed using such methods, in terms of the effects on air-sea exchange of CO_2 . Previous model-based work that considered the distribution and number of platforms needed to constrain air-sea fluxes in the Southern Ocean found that high-frequency variance dominated in topographically complex locations (Mazloff et al., 2018; Wei et al., 2020), suggesting that increased sampling rates in those regions would be a valuable tool for constraining Southern Ocean tracer budgets. Due to the potential importance of these regions in impacting air-sea fluxes, observing systems in the Southern Ocean should consider using an adaptive sampling strategy for these regions, increasing sampling rates when platforms enter these standing meanders. Higher rates of sampling in standing meanders of the ACC may lead to a more complete understanding of their role in the carbon cycle and also provide year-round data regarding strength of subduction and ventilation at the mesoscale and submesoscale.

5. Conclusions

Data from a pair of ocean gliders, deployed alongside a SOCCOM BGC-Argo float, are used to assess the scales of variability in physical and biogeochemical tracers both within and downstream of a major standing meander of the ACC's Polar Front. In both regions, variability in passive tracers is largest along the edge of coherent mesoscale eddies. However, the standing meander, marked by enhanced EKE and strain, exhibits enhanced lateral buoyancy gradients in the mixed layer, a more variable MLD, and evidence of stronger interior mesoscale stirring, as compared to the more quiescent downstream region. Despite similar mean vertical stratification in both parts of the deployment, vertical tracer gradients are nearly an order of magnitude weaker in the standing meander region, suggesting more efficient subduction of surface waters into the interior. While submesoscale motions are likely critical for carrying tracer anomalies across the base of the mixed layer, interior stirring effectively advects these tracers to depth in the standing meander.

The observations presented here confirm a series of recent high-resolution modeling studies (Bachman & Klocker, 2020; Balwada et al., 2018; Rosso et al., 2015) that highlighted the key role that the complex 3D stirring occurs downstream of the interaction of the PF with topography has on vertical exchange between the surface ocean and interior. These regions are characterized as having an active submesoscale flow field with vigorous restratification processes occurring in a region of high EKE. Filamentary structures that allow for the vertical movement of tracers impact the transport of organic matter into the interior ocean, as well as the ventilation of older waters found at depth in the Southern Ocean. There are a discrete number of standing meanders associated with high EKE along the path of the ACC, each of which is likely to be a key region of surface-interior exchange that impacts air-sea exchange and biogeochemical cycling. Our results highlight the need for improved focus on parameterizing flow-topography interactions in models with coarse resolution. Ventilation in the ACC's standing meanders is highly localized, typically spanning a region of only a few hundred kilometers, in which Lagrangian floats experience a short residence time, even with a 1,000-m parking depth. To address the impact of standing meanders on large-scale air-sea carbon fluxes in the Southern Ocean, current and future observational systems should consider employing adaptive sampling in these regions.

Data Availability Statement

The glider data are archived at NOAA's National Centers for Environmental information and can be accessed at <https://www.ncei.noaa.gov/archive/accession/0228185> and <https://www.ncei.noaa.gov/archive/accession/0228187>. Data from the BGC-Argo float were collected and made freely available by the Southern Ocean Carbon and Climate Observations and Modeling (SOCCOM) Project funded by the National Science Foundation, Division of Polar Programs (NSF PLR-1425989 and OPP-1936222), supplemented by NASA, and by the International Argo Program and the NOAA programs that contribute to it (<http://www.argo.ucsd.edu>, <http://argo.jcommops.org>). The Argo Program is part of the Global Ocean Observing System.

Acknowledgments

The authors are grateful to the captain and crew of the R/V Thomas G. Thompson as well as A. Orsi, L. Talley, I. Rosso, G. Viglione, and M. Kotz for their assistance in deploying the gliders during the 2019 I06S GO-SHIP cruise. The authors thank D. Swift, S. Riser, and the SOCCOM executive team for increasing sampling frequency of the BGC-Argo float during the SOGOS mission. LAD and AFT were supported by NSF award OCE-1756956, the David and Lucille Packard Foundation, and the Resnick Sustainability Institute. LAD was additionally supported by an NSF Graduate Research Fellowship. DB and ARG were supported by NSF award OCE-1756882; ARG received additional support from NASA through award NNX80NSSC19K1252 and from the U.S. Argo Program through NOAA grant NA15OAR4320063.

References

- Adams, K. A., Hosegood, P., Taylor, J. R., Sallée, J.-B., Bachman, S., Torres, R., & Stamper, M. (2017). Frontal circulation and submesoscale variability during the formation of a Southern Ocean mesoscale eddy. *Journal of Physical Oceanography*, 47(7), 1737–1753. <https://doi.org/10.1175/JPO-D-16-0266.1>
- Bachman, S. D., & Klocker, A. (2020). Interaction of jets and submesoscale dynamics leads to rapid ocean ventilation. *Journal of Physical Oceanography*, 50(10), 2873–2883. <https://doi.org/10.1175/JPO-D-20-0117.1>
- Bachman, S. D., Taylor, J. R., Adams, K. A., & Hosegood, P. J. (2017). Mesoscale and submesoscale effects on mixed layer depth in the Southern Ocean. *Journal of Physical Oceanography*, 47(9), 2173–2188. <https://doi.org/10.1175/JPO-D-17-0034.1>
- Balwada, D., LaCasce, J. H., Speer, K. G., & Ferrari, R. (2020). Relative dispersion in the Antarctic circumpolar current. *Journal of Physical Oceanography*, 51(2), 553–574. <https://doi.org/10.1175/JPO-D-19-0243.1>
- Balwada, D., Smith, K. S., & Abernathey, R. (2018). Submesoscale vertical velocities enhance tracer subduction in an idealized Antarctic circumpolar current. *Geophysical Research Letters*, 45(18), 9790–9802. <https://doi.org/10.1029/2018GL079244>
- Balwada, D., Speer, K. G., LaCasce, J. H., Owens, W. B., Marshall, J., & Ferrari, R. (2016). Circulation and stirring in the southeast Pacific Ocean and the scotia sea sectors of the Antarctic circumpolar current. *Journal of Physical Oceanography*, 46(7), 2005–2027. <https://doi.org/10.1175/JPO-D-15-0207.1>
- Boccaletti, G., Ferrari, R., & Fox-Kemper, B. (2007). Mixed layer instabilities and restratification. *Journal of Physical Oceanography*, 37(9), 2228–2250. <https://doi.org/10.1175/JPO3101.1>
- Bol, R., Henson, S. A., Rumyantseva, A., & Briggs, N. (2018). High-frequency variability of small-particle carbon export flux in the North-east Atlantic. *Global Biogeochemical Cycles*, 32(12), 1803–1814. <https://doi.org/10.1029/2018GB005963>

- Boyd, P. W., Claustre, H., Levy, M., Siegel, D. A., & Weber, T. (2019). Multi-faceted particle pumps drive carbon sequestration in the ocean. *Nature*, *568*(7752), 327–335. <https://doi.org/10.1038/s41586-019-1098-2>
- Brannigan, L. (2016). Intense submesoscale upwelling in anticyclonic eddies. *Geophysical Research Letters*, *43*(7), 3360–3369. <https://doi.org/10.1002/2016GL067926>
- Briggs, N., Dall'Olmo, G., & Claustre, H. (2020). Major role of particle fragmentation in regulating biological sequestration of CO₂ by the oceans. *Science*, *367*(6479), 791–793. <https://doi.org/10.1126/science.aay1790>
- Briggs, N., Perry, M. J., Cetinić, I., Lee, C., D'Asaro, E., Gray, A. M., & Rehm, E. (2011). High-resolution observations of aggregate flux during a sub-polar North Atlantic spring bloom. *Deep Sea Research Part I: Oceanographic Research Papers*, *58*(10), 1031–1039. <https://doi.org/10.1016/j.dsr.2011.07.007>
- Buesseler, K. O., & Boyd, P. W. (2009). Shedding light on processes that control particle export and flux attenuation in the twilight zone of the open ocean. *Limnology & Oceanography*, *54*(4), 1210–1232. <https://doi.org/10.4319/lo.2009.54.4.1210>
- Dall'Olmo, G., Dingle, J., Polimene, L., Brewin, R. J. W., & Claustre, H. (2016). Substantial energy input to the mesopelagic ecosystem from the seasonal mixed-layer pump. *Nature Geoscience*, *9*(11), 820–823. <https://doi.org/10.1038/ngeo2818>
- de Baar, H. J. W., de Jong, J. T. M., Nolting, R. F., Timmermans, K. R., van Leeuwe, M. A., Bathmann, U., et al. (1999). Low dissolved Fe and the absence of diatom blooms in remote Pacific waters of the Southern Ocean. *Marine Chemistry*, *66*(1), 1–34. [https://doi.org/10.1016/S0304-4203\(99\)00022-5](https://doi.org/10.1016/S0304-4203(99)00022-5)
- Dever, M., Nicholson, D., Omand, M., & Mahadevan, A. (2021). Size-differentiated export flux in different dynamical regimes in the ocean. *Global Biogeochemical Cycles*, *35*(3), e2020GB006764. <https://doi.org/10.1029/2020gb006764>
- Dong, S., Sprintall, J., Gille, S. T., & Talley, L. (2008). Southern Ocean mixed-layer depth from Argo float profiles. *Journal of Geophysical Research: Oceans*, *113*(C6). <https://doi.org/10.1029/2006jc004051>
- Dufour, C. O., Griffies, S. M., de Souza, G. F., Frenger, I., Morrison, A. K., Palter, J. B., et al. (2015). Role of mesoscale eddies in cross-frontal transport of heat and biogeochemical tracers in the Southern Ocean. *Journal of Physical Oceanography*, *45*(12), 3057–3081. <https://doi.org/10.1175/JPO-D-14-0240.1>
- du Plessis, M., Swart, S., Anson, I. J., & Mahadevan, A. (2017). Submesoscale processes promote seasonal restratification in the Subantarctic Ocean. *Journal of Geophysical Research: Oceans*, *122*(4), 2960–2975. <https://doi.org/10.1002/2016JC012494>
- du Plessis, M., Swart, S., Anson, I. J., Mahadevan, A., & Thompson, A. F. (2019). Southern Ocean seasonal restratification delayed by submesoscale wind-front interactions. *Journal of Physical Oceanography*, *49*(4), 1035–1053. <https://doi.org/10.1175/JPO-D-18-0136.1>
- Freeman, N. M., Lovenduski, N. S., Munro, D. R., Krumhardt, K. M., Lindsay, K., Long, M. C., & MacLennan, M. (2018). The variable and changing Southern Ocean silicate front: Insights from the CESM large ensemble. *Global Biogeochemical Cycles*, *32*(5), 752–768. <https://doi.org/10.1029/2017GB005816>
- Freilich, M. A., & Mahadevan, A. (2019). Decomposition of vertical velocity for nutrient transport in the upper Ocean. *Journal of Physical Oceanography*, *49*(6), 1561–1575. <https://doi.org/10.1175/JPO-D-19-0002.1>
- Frölicher, T. L., Sarmiento, J. L., Paynter, D. J., Dunne, J. P., Krasting, J. P., & Winton, M. (2015). Dominance of the Southern Ocean in anthropogenic carbon and heat uptake in CMIP5 models. *Journal of Climate*, *28*(2), 862–886. <https://doi.org/10.1175/JCLI-D-14-00117.1>
- Giddy, I., Swart, S., du Plessis, M., Thompson, A. F., & Nicholson, S.-A. (2021). Stirring of sea-ice meltwater enhances submesoscale fronts in the Southern Ocean. *Journal of Geophysical Research: Oceans*, *126*(4), e2020JC016814. <https://doi.org/10.1029/2020jc016814>
- Gille, S. T., & Kelly, K. A. (1996). Scales of spatial and temporal variability in the Southern Ocean. *Journal of Geophysical Research*, *101*(C4), 8759–8773. <https://doi.org/10.1029/96JC00203>
- Gray, A. R., Johnson, K. S., Bushinsky, S. M., Riser, S. C., Russell, J. L., Talley, L. D., et al. (2018). Autonomous biogeochemical floats detect significant carbon dioxide outgassing in the high-latitude Southern Ocean. *Geophysical Research Letters*, *45*(17), 9049–9057. <https://doi.org/10.1029/2018GL078013>
- Gruber, N., Landschützer, P., & Lovenduski, N. S. (2019). The variable southern ocean carbon sink. *Annual Review of Marine Science*, *11*(1), 159–186. <https://doi.org/10.1146/annurev-marine-121916-063407>
- Haëntjens, N., Boss, E., & Talley, L. D. (2017). Revisiting ocean color algorithms for chlorophyll a and particulate organic carbon in the Southern Ocean using biogeochemical floats. *Journal of Geophysical Research: Oceans*, *122*(8), 6583–6593. <https://doi.org/10.1002/2017jc012844>
- Johnson, K. S., Coletti, L. J., Jannasch, H. W., Sakamoto, C. M., Swift, D. D., & Riser, S. C. (2013). Long-term nitrate measurements in the ocean using the in situ ultraviolet spectrophotometer: Sensor integration into the APEX profiling float. *Journal of Atmospheric and Oceanic Technology*, *30*(8), 1854–1866. <https://doi.org/10.1175/jtech-d-12-00221.1>
- Johnson, K. S., Jannasch, H. W., Coletti, L. J., Elrod, V. A., Martz, T. R., Takeshita, Y., et al. (2016). Deep-sea DuraFET: A pressure tolerant pH sensor designed for global sensor networks. *Analytical Chemistry*, *88*(6), 3249–3256. <https://doi.org/10.1021/acs.analchem.5b0465310.1021/acs.analchem.5b04653>
- Johnson, K. S., Plant, J. N., Coletti, L. J., Jannasch, H. W., Sakamoto, C. M., Riser, S. C., et al. (2017). Biogeochemical sensor performance in the SOCCOM profiling float array. *Journal of Geophysical Research: Oceans*, *122*(8), 6416–6436. <https://doi.org/10.1002/2017JC012838>
- Johnson, K. S., Plant, J. N., Riser, S. C., & Gilbert, D. (2015). Air oxygen calibration of oxygen optodes on a profiling float array. *Journal of Atmospheric and Oceanic Technology*, *32*(11), 2160–2172. <https://doi.org/10.1175/JTECH-D-15-0101.1>
- Joyce, T. M., Zenk, W., & Toole, J. M. (1978). The anatomy of the Antarctic polar front in the Drake Passage. *Journal of Geophysical Research*, *83*, 6093–6113. <https://doi.org/10.1029/jc083ic12p06093>
- Kim, Y. S., & Orsi, A. H. (2014). On the variability of Antarctic circumpolar current fronts inferred from 1992–2011 Altimetry. *Journal of Physical Oceanography*, *44*(12), 3054–3071. <https://doi.org/10.1175/JPO-D-13-0217.1>
- Klein, P., & Lapeyre, G. (2009). The oceanic vertical pump induced by mesoscale and submesoscale turbulence. *Annual Review of Marine Science*, *1*(1), 351–375. <https://doi.org/10.1146/annurev.marine.010908.163704>
- Kostadinov, T. S., Siegel, D. A., & Maritorena, S. (2009). Retrieval of the particle size distribution from satellite ocean color observations. *Journal of Geophysical Research*, *114*(C9). <https://doi.org/10.1029/2009JC005303>
- Levy, M., Bopp, L., Karleskind, P., Resplandy, L., Ethe, C., & Pinsard, F. (2013). Physical pathways for carbon transfers between the surface mixed layer and the ocean interior. *Global Biogeochemical Cycles*, *27*(4), 1001–1012. <https://doi.org/10.1002/gbc.20092>
- Lévy, M., Ferrari, R., Franks, P. J. S., Martin, A. P., & Rivière, P. (2012). Bringing physics to life at the submesoscale. *Geophysical Research Letters*, *39*(14). <https://doi.org/10.1029/2012GL052756>
- Lévy, M., Franks, P. J. S., & Smith, K. S. (2018). The role of submesoscale currents in structuring marine ecosystems. *Nature Communications*, *9*(1), 4758. <https://doi.org/10.1038/s41467-018-07059-3>
- Llort, J., Langlais, C., Matear, R., Moreau, S., Lenton, A., & Strutton, P. G. (2018). Evaluating southern ocean carbon eddy-pump from biogeochemical-Argo floats. *Journal of Geophysical Research: Oceans*, *123*(2), 971–984. <https://doi.org/10.1002/2017JC012861>

- Loisel, H., Nicolas, J.-M., Sciandra, A., Stramski, D., & Poteau, A. (2006). Spectral dependency of optical backscattering by marine particles from satellite remote sensing of the global ocean. *Journal of Geophysical Research*, 111(C9). <https://doi.org/10.1029/2005JC003367>
- Lu, J., & Speer, K. (2010). Topography, jets and eddy mixing in the Southern Ocean. *Journal of Marine Research*, 68, 479–502. <https://doi.org/10.1357/002224010794657227>
- Lu, J., Wang, F., Liu, H., & Lin, P. (2016). Stationary mesoscale eddies, upgradient eddy fluxes, and the anisotropy of eddy diffusivity. *Geophysical Research Letters*, 43(2), 743–751. <https://doi.org/10.1002/2015GL067384>
- MacCready, P., & Rhines, P. B. (2001). Meridional transport across a zonal channel: Topographic localization. *Journal of Physical Oceanography*, 31, 1427–1439. [https://doi.org/10.1175/1520-0485\(2001\)031<1427:mtaazc>2.0.co;2](https://doi.org/10.1175/1520-0485(2001)031<1427:mtaazc>2.0.co;2)
- Mahadevan, A. (2016). The impact of submesoscale physics on primary productivity of plankton. *Annual Review of Marine Science*, 8(1), 161–184. <https://doi.org/10.1146/annurev-marine-010814-015912>
- Marshall, J., & Speer, K. (2012). Closure of the meridional overturning circulation through Southern Ocean upwelling. *Nature Geoscience*, 5(3), 171–180. <https://doi.org/10.1038/ngeo1391>
- Mazloff, M. R., Cornuelle, B. D., Gille, S. T., & Verdy, A. (2018). Correlation lengths for estimating the large-scale carbon and heat content of the Southern Ocean. *Journal of Geophysical Research: Oceans*, 123(2), 883–901. <https://doi.org/10.1002/2017jc013408>
- McDougall, T. J., & Barker, P. M. (2011). Getting started with TEOS-10 and the Gibbs seawater (GSW) oceanographic toolbox. *SCOR/LAPSO WG*, 127, 1–28.
- McWilliams, J. C. (2016). Submesoscale currents in the ocean. *Proceedings of the Royal Society A: Mathematical, Physical & Engineering Sciences*, 472(2189), 20160117. <https://doi.org/10.1098/rspa.2016.0117>
- Meredith, M. P., Schofield, O., Newman, L., Urban, E., & Sparrow, M. (2013). The vision for a Southern Ocean observing system. *Current Opinion in Environmental Sustainability*, 5, 306–313. <https://doi.org/10.1016/j.cosust.2013.03.002>
- Naveira Garabato, A. C., Ferrari, R., & Polzin, K. L. (2011). Eddy stirring in the Southern Ocean. *Journal of Geophysical Research*, 116, C09019. <https://doi.org/10.1029/2010jc006818>
- Omand, M. M., D'Asaro, E. A., Lee, C. M., Perry, M. J., Briggs, N., Cetinić, I., & Mahadevan, A. (2015). Eddy-driven subduction exports particulate organic carbon from the spring bloom. *Science*, 348(6231), 222–225. <https://doi.org/10.1126/science.1260062>
- Orsi, A. H., Whitworth, T., & Nowlin, W. D. (1995). On the meridional extent and fronts of the Antarctic Circumpolar Current. *Deep Sea Research Part I: Oceanographic Research Papers*, 42(5), 641–673. [https://doi.org/10.1016/0967-0637\(95\)00021-W](https://doi.org/10.1016/0967-0637(95)00021-W)
- Palevsky, H. I., Quay, P. D., Lockwood, D. E., & Nicholson, D. P. (2016). The annual cycle of gross primary production, net community production, and export efficiency across the North Pacific Ocean. *Global Biogeochemical Cycles*, 30(2), 361–380. <https://doi.org/10.1002/2015GB005318>
- Pollard, R. T., & Read, J. F. (2001). Circulation pathways and transports of the Southern Ocean in the vicinity of the Southwest Indian Ridge. *Journal of Geophysical Research*, 106, 2881–2898. <https://doi.org/10.1029/2000jc900090>
- Rintoul, S. R. (2018). The global influence of localized dynamics in the Southern Ocean. *Nature*, 558(7709), 209–218. <https://doi.org/10.1038/s41586-018-0182-3>
- Rintoul, S. R., & Naveira Garabato, A. C. (2013). Chapter 18—Dynamics of the Southern Ocean circulation. In G. Siedler, S. M. Griffies, J. Gould, & J. A. Church (Eds.), *International Geophysics* (Vol. 103, pp. 471–492). Academic Press. <https://doi.org/10.1016/B978-0-12-391851-2.00018-0>
- Riser, S. C., Freeland, H. J., Roemmich, D., Wijffels, S., Troisi, A., Belbéoch, M., et al. (2016). Fifteen years of ocean observations with the global Argo array. *Nature Climate Change*, 6(2), 145–153. <https://doi.org/10.1038/nclimate2872>
- Roach, C. J., Balwada, D., & Speer, K. (2016). Horizontal mixing in the Southern Ocean from Argo float trajectories. *Journal of Geophysical Research: Oceans*, 121(8), 5570–5586. <https://doi.org/10.1002/2015JC011440>
- Roemmich, D., & Gilson, J. (2009). The 2004–2008 mean and annual cycle of temperature, salinity, and steric height in the global ocean from the Argo Program. *Progress in Oceanography*, 82(2), 81–100. <https://doi.org/10.1016/j.poccean.2009.03.004>
- Rosso, I., Hogg, A. M., Kiss, A. E., & Gayen, B. (2015). Topographic influence on submesoscale dynamics in the Southern Ocean. *Geophysical Research Letters*, 42(4), 1139–1147. <https://doi.org/10.1002/2014GL062720>
- Rosso, I., Hogg, A. M., Strutton, P. G., Kiss, A. E., Matear, R., Klocker, A., & van Sebille, E. (2014). Vertical transport in the ocean due to sub-mesoscale structures: Impacts in the Kerguelen region. *Ocean Modelling*, 80, 10–23. <https://doi.org/10.1016/j.ocemod.2014.05.001>
- Rousseaux, C. S., & Gregg, W. W. (2014). Interannual variation in phytoplankton primary production at a global scale. *Remote Sensing*, 6(1), 1–19. <https://doi.org/10.3390/rs6010001>
- Ruiz, S., Pascual, A., Garau, B., Pujol, I., & Tintoré, J. (2009). Vertical motion in the upper ocean from glider and altimetry data. *Geophysical Research Letters*, 36(14). <https://doi.org/10.1029/2009GL038569>
- Sallée, J.-B., Matear, R. J., Rintoul, S. R., & Lenton, A. (2012). Localized subduction of anthropogenic carbon dioxide in the Southern Hemisphere oceans. *Nature Geoscience*, 5(8), 579–584. <https://doi.org/10.1038/ngeo1523>
- Schlitzer, R. (2002). Carbon export fluxes in the Southern Ocean: Results from inverse modeling and comparison with satellite-based estimates. *Deep Sea Research Part II: Topical Studies in Oceanography*, 49(9), 1623–1644. [https://doi.org/10.1016/S0967-0645\(02\)00004-8](https://doi.org/10.1016/S0967-0645(02)00004-8)
- Siegelman, L. (2020). Energetic submesoscale dynamics in the ocean interior. *Journal of Physical Oceanography*, 50(3), 727–749. <https://doi.org/10.1175/JPO-D-19-0253.1>
- Siegelman, L., Klein, P., Rivière, P., Thompson, A. F., Torres, H. S., Flexas, M., & Menemenlis, D. (2020). Enhanced upward heat transport at deep submesoscale ocean fronts. *Nature Geoscience*, 13(1), 50–55. <https://doi.org/10.1038/s41561-019-0489-1>
- Siegelman, L., O'Toole, M., Flexas, M., Rivière, P., & Klein, P. (2019). Submesoscale ocean fronts act as biological hotspot for southern elephant seal. *Scientific Reports*, 9(1), 1–13. <https://doi.org/10.1038/s41598-019-42117-w>
- Smith, K. S., & Ferrari, R. (2009). The production and dissipation of compensated thermohaline variance by mesoscale stirring. *Journal of Physical Oceanography*, 39(10), 2477–2501. <https://doi.org/10.1175/2009JPO4103.1>
- Sokolov, S., & Rintoul, S. R. (2009). Circumpolar structure and distribution of the Antarctic Circumpolar Current fronts: 1. Mean circumpolar paths. *Journal of Geophysical Research*, 114(C11). <https://doi.org/10.1029/2008JC005108>
- Stewart, K. D., & Haine, T. W. N. (2016). Thermobaricity in the transition zones between alpha and beta oceans. *Journal of Physical Oceanography*, 46(6), 1805–1821. <https://doi.org/10.1175/JPO-D-16-0017.1>
- Stukel, M. R., Aluwihare, L. I., Barbeau, K. A., Chekalyuk, A. M., Goericke, R., Miller, A. J., et al. (2017). Mesoscale ocean fronts enhance carbon export due to gravitational sinking and subduction. *Proceedings of the National Academy of Sciences*, 114(6), 1252–1257. <https://doi.org/10.1073/pnas.1609435114>
- Stukel, M. R., & Ducklow, H. W. (2017). Stirring up the biological pump: Vertical mixing and carbon export in the Southern Ocean. *Global Biogeochemical Cycles*, 31(9), 1420–1434. <https://doi.org/10.1002/2017GB005652>

- Su, Z., Wang, J., Klein, P., Thompson, A. F., & Menemenlis, D. (2018). Ocean submesoscales as a key component of the global heat budget. *Nature Communications*, 9(1), 775. <https://doi.org/10.1038/s41467-018-02983-w>
- Sutton, A. J., Williams, N. L., & Tilbrook, B. (2021). Constraining Southern Ocean CO₂ flux uncertainty using uncrewed surface vehicle observations. *Geophysical Research Letters*, 48(3), e2020GL091748. <https://doi.org/10.1029/2020GL091748>
- Swart, S., du Plessis, M. D., Thompson, A. F., Biddle, L. C., Giddy, I., Linders, T., et al. (2020). Submesoscale fronts in the Antarctic marginal ice zone and their response to wind forcing. *Geophysical Research Letters*, 47(6), e2019GL086649. <https://doi.org/10.1029/2019GL086649>
- Tamsitt, V., Drake, H. F., Morrison, A. K., Talley, L. D., Dufour, C. O., Gray, A. R., et al. (2017). Spiraling pathways of global deep waters to the surface of the Southern Ocean. *Nature Communications*, 8(1), 1–10. <https://doi.org/10.1038/s41467-017-00197-0>
- Tengberg, A., Hovdenes, J., Andersson, H. J., Brocandel, O., Diaz, R., Hebert, D., et al. (2006). Evaluation of a lifetime-based optode to measure oxygen in aquatic systems. *Limnology and Oceanography: Methods*, 4(2), 7–17. <https://doi.org/10.4319/lom.2006.4.7>
- Thomas, L. N., & Lee, C. M. (2005). Intensification of ocean fronts by down-front winds. *Journal of Physical Oceanography*, 35(6), 1086–1102. <https://doi.org/10.1175/JPO2737.1>
- Thomas, L. N., Tandon, A., & Mahadevan, A. (2008). *Submesoscale processes and dynamics*, *Geophysical Monograph Series* (Vol. 177, pp. 17–38). Washington DC: American Geophysical Union. <https://doi.org/10.1029/177GM04>
- Thompson, A. F., Lazar, A., Buckingham, C., Naveira Garabato, A. C., Damerell, G. M., & Heywood, K. J. (2016). Open-ocean submesoscale motions: A full seasonal cycle of mixed layer instabilities from gliders. *Journal of Physical Oceanography*, 46(4), 1285–1307. <https://doi.org/10.1175/JPO-D-15-0170.1>
- Thompson, A. F., & Naveira Garabato, A. C. (2014). Equilibration of the Antarctic Circumpolar Current by standing meanders. *Journal of Physical Oceanography*, 44(7), 1811–1828. <https://doi.org/10.1175/JPO-D-13-0163.1>
- Thompson, A. F., & Sallée, J.-B. (2012). Jets and topography: Jet transitions and the impact on transport in the Antarctic Circumpolar Current. *Journal of Physical Oceanography*, 42(6), 956–972. <https://doi.org/10.1175/JPO-D-11-0135.1>
- Uchida, T., Balwada, D., Abernathy, R., McKinley, G., Smith, S., & Lévy, M. (2019). The contribution of submesoscale over mesoscale eddy iron transport in the open Southern Ocean. *Journal of Advances in Modeling Earth Systems*, 11(12), 3934–3958. <https://doi.org/10.1029/2019MS001805>
- Vaillancourt, R. D., Brown, C. W., Guillard, R. R. L., & Balch, W. M. (2004). Light backscattering properties of marine phytoplankton: Relationships to cell size, chemical composition and taxonomy. *Journal of Plankton Research*, 26(2), 191–212. <https://doi.org/10.1093/plankt/fbh012>
- Viglione, G. A., & Thompson, A. F. (2016). Lagrangian pathways of upwelling in the Southern Ocean. *Journal of Geophysical Research: Oceans*, 121(8), 6295–6309. <https://doi.org/10.1002/2016JC011773>
- Viglione, G. A., Thompson, A. F., Flexas, M. M., Sprintall, J., & Swart, S. (2018). Abrupt transitions in submesoscale structure in southern Drake Passage: Glider observations and model results. *Journal of Physical Oceanography*, 48(9), 2011–2027. <https://doi.org/10.1175/JPO-D-17-0192.1>
- Wei, Y., Gille, S. T., Mazloff, M. R., Tamsitt, V., Swart, S., Chen, D., & Newman, L. (2020). Optimizing mooring placement to constrain southern ocean air-sea fluxes. *Journal of Atmospheric and Oceanic Technology*, 37(8), 1365–1385. <https://doi.org/10.1175/jtech-d-19-0203.1>
- Witter, D. L., & Chelton, D. B. (1998). Eddy-mean flow interaction in zonal oceanic jet flow along zonal ridge topography. *Journal of Physical Oceanography*, 28. [https://doi.org/10.1175/1520-0485\(1998\)028<2019:emfiiz>2.0.co;2](https://doi.org/10.1175/1520-0485(1998)028<2019:emfiiz>2.0.co;2)
- Youngs, M. K., Thompson, A. F., Lazar, A., & Richards, K. J. (2017). ACC meanders, energy transfer, and mixed barotropic-baroclinic instability. *Journal of Physical Oceanography*, 47(6), 1291–1305. <https://doi.org/10.1175/JPO-D-16-0160.1>
- Zhang, X., Hu, L., & He, M.-X. (2009). Scattering by pure seawater: Effect of salinity. *Optics Express*, 17(7), 5698–5710. <https://doi.org/10.1364/OE.17.005698>